Chem Soc Rev

REVIEW ARTICLE

View Article Online
View Journal | View Issue

Cite this: *Chem. Soc. Rev.*, 2016, **45**, 1935

Fundamental developments in infrared spectroscopic imaging for biomedical applications

Michael Pilling and Peter Gardner*

Infrared chemical imaging is a rapidly emerging field with new advances in instrumentation, data acquisition and data analysis. These developments have had significant impact in biomedical applications and numerous studies have now shown that this technology offers great promise for the improved diagnosis of the diseased state. Relying on purely biochemical signatures rather than contrast from exogenous dyes and stains, infrared chemical imaging has the potential to revolutionise histopathology for improved disease diagnosis. In this review we discuss the recent advances in infrared spectroscopic imaging specifically related to spectral histopathology (SHP) and consider the current state of the field. Finally we consider the practical application of SHP for disease diagnosis and consider potential barriers to clinical translation highlighting current directions and the future outlook.

Received 10th November 2015

DOI: 10.1039/c5cs00846h

www.rsc.org/chemsocrev

Introduction

Since its inception histopathology, the microscopic study of diseased tissue, has relied on optical microscopy as the principle means of analysing the sample. Optical brightfield microscopy has indeed flourished, and is ubiquitous in pathology laboratories worldwide, and remains the 'gold standard' for classification of the disease state. Conventional optical microscopy relies on the interaction of light with matter, and the observed contrast provides information relating to sample morphology alone. However, tissue generally exhibits poor contrast and this has led to the introduction of a wide range of different types of stains to highlight certain tissue and cell types and aid the pathologist in diagnosis. Hematoxylin and eosin is the principle stain used

Manchester Institute of Biotechnology, University of Manchester, 131 Princess Street, Manchester, M1 7DN, UK. E-mail: Peter.Gardner@Manchester.ac.uk; Fax: +44 (0)161 306 5201; Tel: +44 (0)161 306 4463

Michael Pilling

Michael Pilling obtained his PhD in Chemistry from the University of Manchester Institute of Science and Technology under the supervision of Professor Peter Gardner. Following his PhD he undertook his first postdoctoral position with Professor Carol Hirschmugl at the National Synchrotron Light Source, Brookhaven National Laboratory, New York, USA. In 2005 he worked at GlaxoSmithKline in the Process Analytical Technology and Chemometrics group, utilising real-time in situ spectroscopy in plant for improved process understanding and control. Currently he holds a postdoctoral position with Professor Peter Gardner where he is investigating the improved diagnosis of prostate cancer using infrared hyperspectral imaging.

Peter Gardner

Peter Gardner studied chemistry at the University of East Anglia and obtained his PhD in physical chemistry 1988. He then spent four years as a postdoctoral researcher at the Fritz-Haber Institute in Berlin where he applied vibrational spectroscopy to study molecular adsorption of surfaces. In 1992 moved to the Chemistry Department in Cambridge and in 1994 he was appointed as a lecturer in the Department of Chemistry at the University of Manchester Institute of Science and Technology. Here he started working on synchrotron-based infrared microscopy and he did his first work on biological systems. In 2004 he joined the School of Chemical Engineering and Analytical Science at the University of Manchester and was appointed Chair of Analytical and Biomedical Spectroscopy in 2012. Since 2006 his research group have been based at the Manchester Institute of Biotechnology.

in histopathology, staining protein rich regions pink and nucleic acid rich regions blue, enabling superior tissue differentiation. Microscopic analysis of stained tissue provides the pathologist with a high level of information often enabling accurate determination of the disease state and the likely prognosis for the patient. However manual examination of tissue sections is a laborious and often a time consuming process and there can be significant delays between a tissue biopsy being obtained and diagnosis being made, with clear implications for patient treatment and care. Furthermore diagnosis is based essentially on tissue morphology and architecture alone, and is therefore highly subjective and susceptible to both inter and intra observer error.[1,2] Immunohistochemistry improves chemical (protein) specificity but the process is time consuming and is normally restricted to one stain per sample. In an attempt to increase sample throughput and objectivity, machine learning and pattern recognition H&E analysis techniques have been investigated by a number of researchers.[3,4] Although there has been some progress in this area, no such clinical protocols are currently in place and manual examination is the norm.

Technological advances during the last decade have resulted in the proliferation of a new and exciting family of techniques collectively known as chemical imaging.[5–7] Contrast in chemical imaging is provided purely by sample chemical composition rather than morphology alone, enabling representation of an image as a function of sample chemical identity. Recently, infrared chemical imaging for disease diagnostics has gained attention as a rapidly emerging technology within the biomedical field,[8–14] combining the high spatial resolution of microscopy with infrared spectroscopy to provide spatially resolved infrared spectra. Progress in this area has been driven by infrared spectroscopy being a well established technique utilising the interaction of infrared radiation with molecular vibrations within tissue to produce unique spectral signatures.[15] Infrared spectra from biological material are broadly similar containing absorption bands due to proteins, carbohydrates and lipids. A typical infrared absorption spectrum highlighting the principle bands is shown in Fig. 1.

Biological material can be interrogated with this technique to provide a biochemical fingerprint of the tissue with little or no sample preparation and without the need for exogenous labelling. These developments have led to the emergence of a promising new diagnostic field, utilising spectral measurements of tissue to highlight biochemical differences between normal, predeceased (often termed preclinical) and the diseased state. This review focuses on recent advances in infrared imaging in the context of spectral histopathology (SHP), and examines the current state of the technology and considers future barriers to implementation as a clinical diagnostic tool.

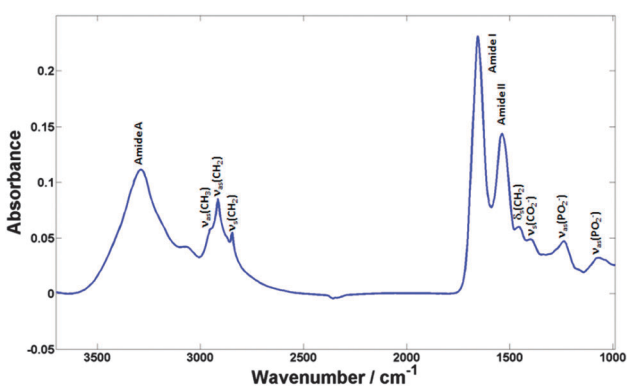

Fig. 1 A typical FTIR microscopy spectrum of tissue obtained from a 4 μm prostate section.

Instrumentation

As early as the 1950's attempts were being made to use infrared microscopy to investigate biological material. In Barer's seminal paper[16] he discussed the limitations of the technology at the time which relied on a dispersive infrared spectrophotometer coupled to a reflecting microscope known as the Burch microscope. Barer was acutely aware that the technology was in its infancy and commented that source power, detector efficiency, spectrometer throughput and resolving power were all confounding factors, and recognised improvements needed to be made if it was to be applied more widely. The first commercially available infrared microscope was produced by Perkin Elmer in 1953, based on a design by Coates,[17] which consisted of a microscope accessory coupled to a dispersive infrared spectrometer. The spatial resolution of the instrument was limited by the available energy at a given wavelength, often requiring long pathlengths, and excessive scan times to obtain reasonable signal to noise ratios. Despite this, Coates was able to publish an infrared spectrum of a 25 μm thick section of rat brain tissue over a narrow spectral range (7–11 μm). During the following two decades limited advances were made in infrared microscopy technology and it remained a highly specialised research technique with limited applications. Advances in computing during the 1980's led to the availability of commercial high throughput Fourier transform infrared (FTIR) spectrometers and this resulted in renewed interest in infrared microscopy. Despite this, infrared microscopes remained a bolt on accessory and therefore were not fully optimised to the FTIR to which they were coupled to and this limited system performance. Later integrated FTIR microscopy systems became available which matched high throughput state of the art spectrometers to high precision infrared microscopes, resulting in the reliable, high performance, instruments commonly in use today.

Spectral histopathology of tissue relies on wide field scanning at high spatial resolution over relatively large areas of the sample. Several modes of operation are available for acquiring chemical images of tissue, and the most suitable depends on a number of factors including speed of collection, desired spatial resolution and end user cost. The mostly commonly used IR modes of operation are transmission, transflection, and attenuated total reflection (ATR) Fig. 2. In transmission mode (Fig. 2a) a thin section of tissue, typically 4–12 μm is fixed to the surface of an infrared transmissive slide. Barium fluoride or calcium fluoride substrates are commonly use because they

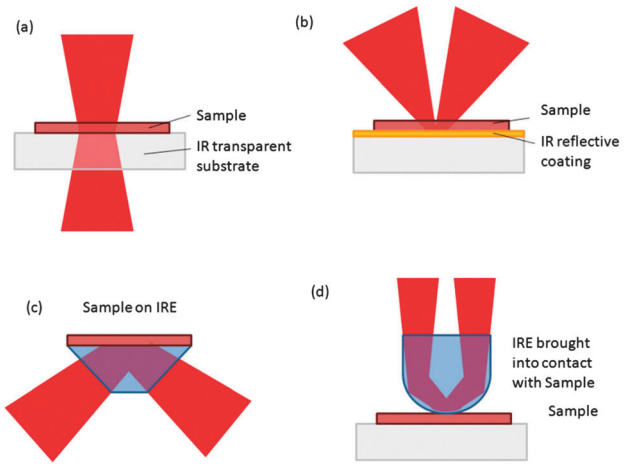

Fig. 2 A schematic diagram indicating the commonly used sampling geometries in SHP. In (a) the sample is on a transparent substrate enabling the IR light to pass through. In (b) the bulk substrate is not transparent to IR but is coated with an infrared reflective coating allowing the infrared beam to pass through the sample, reflect off the substrate surface and pass back through the sample to be collected by the detector. Attenuated total reflection is shown in (c) and (d). In (c) the sample is mounted to an internal reflection element (IRE), and (d) the sample is mounted on a substrate and the IRE brought into intimate contact.

have high transparency in the mid infrared region, although alternative substrates such as zinc selenide or silicon can also be used. Infrared light passes through both the tissue and the infrared transmissive slide, and the transmitted light is measured using an infrared detector. Transflection mode (Fig. 2b), utilises an infrared reflective surface which has the tissue to be interrogated mounted to its surface. Infrared light passes through the tissue, reflects off the reflective layer and passes through the tissue a second time. ATR relies on the formation of an evanescent wave formed when light total internally reflects within a prism. Tissue is mounted onto an ATR prism (Fig. 2c), (typically germanium, zinc selenide or diamond), and the evanescent wave penetrates a finite distance into the tissue. Penetration depth is typically a few microns and depends on wavelength, refractive index of the prism and also the angle of incidence. Alternatively tissue can be mounted onto a substrate and an internal reflection element (IRE) is brought into contact with the tissue (Fig. 2d). ATR has the advantage that since only the first few microns of a sample are measured, thicker tissue sections can used provided there is intimate contact between the tissue and the ATR crystal.

Single point IR microscopy dates back to the earliest commercially available instruments, and utilises a single element detector which records an infrared spectrum from an individual location on the sample. Best suited to interrogating small localised regions of interest, spectra with high signal to noise ratios can routinely be acquired. Spatial resolution in single point mode is defined by the size of the aperture used to reduce the field of view. Imaging large tissue areas requires the beam to be rastered point by point to form a large grid, which can then be stitched together post-collection to form a single chemical image. Since the sample has to be moved following each acquisition point, a significant proportion of collection time is used translating the stage, particularly when mapping large samples. Reduced throughput of light through the aperture coupled with the low brightness of conventional FTIR benchtop sources impacts on signal to noise and often leads to excessive measurement times (hours or even days).[18] Therefore it has generally been common practice to reduce the number of scans acquired for each point and using larger aperture sizes, which effectively limits the spatial resolution to between approximately 20–30 μm. Spectral mixing due to boundary pixels has been discussed by several authors and effectively reduces the usefulness of single point mapping for tissue imaging.[8,19,20] High spatial resolution in single point mode can only be achieved using restrictively small aperture sizes, which can severely restrict throughput for poor collimated infrared sources. The requirement of a highly collimated infrared source for small aperture sizes has led to the use of synchrotron radiation in infrared microscopy. Compared to a conventional thermal source synchrotron radiation is between 100–1000 times brighter,[21] enabling a much higher throughput of light when using reduced aperture sizes. Fig. 3 Compares the mercury cadmium telluride (MCT) detector signal observed using a synchrotron source and also a conventional FTIR globar source as the size of the microscope aperture is reduced. As can be seen, using an aperture of 10 μm the globar results in negligible signal reaching the detector whereas the synchrotron still delivers significant signal.

The highly collimated and inherent brightness of the synchrotron enables high quality spectra at high spatial resolution to be acquired within reasonable acquisition times.[23–27] However synchrotron IR microscopy in single point mode still requires that the sample is rastered to form a complete infrared image. The situation is exacerbated when using small apertures

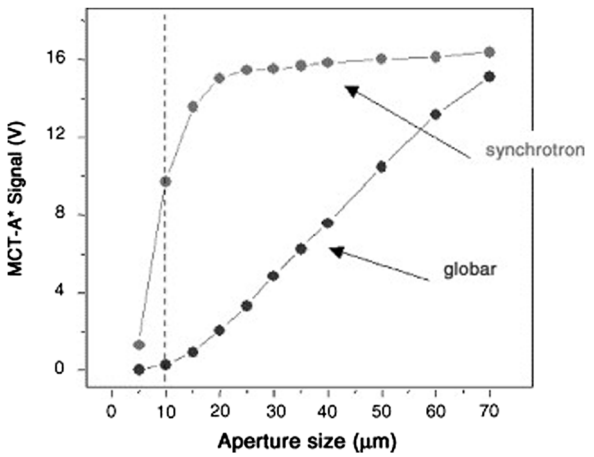

Fig. 3 Infrared signal through various aperture sizes using a synchrotron *vs.* globar source. A confocal IR microscope was used with a single point-detector. With a 10 μm square aperture, most of the synchrotron light passes through, while very little throughput is obtained with the globar source. Reprinted from Vibrational Spectroscopy, **38**(1–2), Lisa M. Miller, Randy J. Smith, Synchrotrons *versus* globars, point-detectors *versus* focal plane arrays: Selecting the best source and detector for specific infrared microspectroscopy and imaging applications, 237–240, Copyright (2005), with permission from Elsevier.[22]

to obtain high spatial resolution, the smaller field of view means a large number of points need to be acquired to image a given area, reducing its usefulness for imaging tissue. SR-FTIR is generally more suited for high resolution (<20 μm) measurements in single point mode, and the majority of research has therefore focussed on cells[27–34] rather than tissue.

Although high quality images are obtainable in single point collection mode, chemical imaging within practical timescales requires the acquisition of multiple surface points simultaneously. Advances in infrared detector technology have revolutionised infrared chemical imaging. Originally designed and developed for defence applications, linear array and focal plane array detectors have now become widely commercially available. In contrast to single element detection, array detectors do not use apertures to restrict the field of view. Microscope optics define the field of view and the image is projected on to an array of individual detectors on a linear array or focal plane. Spatial resolution (up to the diffraction limit) is determined only by the field of view and the number of detectors in the illuminated array. Since no apertures are required to restrict the field of view, higher throughput of light can be obtained compared to single point mapping. Through multiplexing, FPA technology enables each detector in the array to record an infrared spectrum simultaneously. Currently two principle types of array detectors are available. The simplest is the linear array detector, which consists of a row of detector elements (typically 16) in a straight line. The MCT detectors in such arrays work in photoconductive mode and have similar detectivities to the single element MCT detectors. The principle of imaging a sample is similar to that utilised in single point mapping except that multiple rows of spectra can be collected simultaneously significantly reducing acquisition times. The advantage of the small linear array[35] is that the signal readout is fast. Focal plane array detectors usually consist of a square array of infrared detector elements. The detector elements work in photovoltaic mode (rather than photoconductive) and thus have a slightly reduced spectral range with a lower wavenumber cut-off of approximately 850 cm^{-1}.[36] FPA technology has revolutionised infrared chemical imaging since it enables a large number of spectra to be acquired for a sample simultaneously. The pixel size of the chemical image depends on the number of detectors in the array and the microscope optics which in turn defines the field of view. Naturally there is a trade off between the pixel size and signal to noise, typically the microscope optics are matched to the FPA to enable a pixel resolution of approximately 5 μm. Most commercially available FTIR microscopes nowadays utilise a 64 × 64 FPA detector which enables simultaneous acquisition of 4096 spectra. Larger array are available but suffer from relatively slow data readout from the large number of individual elements meaning that the detector duty cycle is low. Nevertheless 128 × 128 FPA detectors are becoming increasingly common. Recent studies have demonstrated that by using a 15× objective coupled to a 128 × 128 FPA[37] tissue areas from a single infrared image (704 μm × 704 μm) can be quickly measured. FPA technology coupling to rapid scanning FTIR has indeed opened up the possibility of large area tissue imaging. Bassan[38] exploited the multiplex advantage of FPA technology to image a full prostate organ section with an approximate area of 40 × 50 mm. The complete chemical image consisted of approximately 66.3 million complete infrared spectra and took just 14 hours to acquire. In a related paper[39] the same author showed that the smaller more routine clinical samples (prostate TURPs) could be imaged, resulting in ~2 million spectra in ~30 min demonstrating that such samples can be measured within practical clinical timescales. If high spatial resolution is not necessary then very rapid imaging can be achieved for large areas using a 4× objective, which give rise to a pixel size of ~19 μm. Beleites *et al.*[40] demonstrated that good classification of laryngeal carcinoma tissue could be achieved from this low spatial resolution data that had been collected in approximately one tenth of the time required using the 15× objective.

High resolution imaging

Despite optical brightfield imaging of stained tissue being the gold standard for disease diagnosis, FTIR chemical imaging is emerging as a potential competitive technique for enhanced disease understanding and improved diagnosis. Considerable progress has been made over the last decade utilising infrared hyperspectral data coupled with machine learning techniques to classify tissue with regards to disease state with high sensitivity and high specificity.[41–45] Translation into the clinic however has been inhibited in part by the available technology lagging behind what is required to be competitive with standard histopathology methods. The field of telepathology, latterly termed digital pathology, is advancing rapidly. Brightfield microscopy has become highly automated and several tissue sections on separate slides can be scanned in a matter of minutes.[46] Advances in infrared detectors utilising FPA technology have significantly reduced acquisition times, but until recently could not compete with the high spatial resolution achievable with optical microscopy. In some cases of suspected cancer examination of micro heterogeneity at the basal membrane is required as this is often the first indication of abnormality. A pathologist will usually first examine gross morphological changes at low magnification, to identify areas of concern before focussing on sub-cellular regions of suspicious tissue. In ambiguous cases of suspected prostate cancer a pathologist will often look for cellular invasion, such as perineural invasion (invasion into a nerve), to enable a conclusive diagnosis. Subtle changes on the cellular level occurring across microscopic membranes requires high quality, high resolution images to be obtained.

Conventional wisdom dictates that there will always be a trade-off between improved spatial resolution and signal to noise. One of the main hurdles to overcome in improved spatial resolution is the diffraction limit, which is often referred to in terms of the Rayleigh criterion (strictly speaking only applicable for a circular aperture) the spatial resolution r is given by $r = 1.22\lambda/(2 \times \mathrm{NA})$, where λ is the wavelength of the radiation in question, NA is the numerical aperture, and $\mathrm{NA} = n \sin\theta$, where n is the refractive index of the medium between the

objective and the sample and θ is the acceptance angle of the objective. Under ideal conditions the optimum achievable spatial resolution will therefore be approximately $1/\lambda$ which for the fingerprint region gives a spatial resolution of between 2.5–5 μm. An infrared microscope operating in transmission mode utilising an FPA will usually operate with a spatial resolution of 5–6 μm to ensure sufficient signal to noise is achievable. Under these conditions it is clear that the spatial resolution obtained is generally poorer than the diffraction limited resolution which can impact on chemical image quality. One potential solution is to operate under an optical configuration where the numerical aperture is increased. The Raleigh criterion states that the diffraction limited resolution is inversely proportion to the numerical aperture so increasing the NA should reduce the diffraction limit for a given wavelength of light. This can be achieved either by increasing the collection angle theta or by increasing the refractive index of the medium through which the light is passing. Kazarian has pioneered the latter methodology,[47–53] using attenuated total reflection (ATR) imaging with ATR crystal (400 μm × 400 μm) with a high refractive index. Using a germanium ATR crystal (with a refractive index of 4.06–4.0 across the mid IR range) delivers an approximate four-fold improvement in spatial resolution. Walsh[54] has also exploited this effect enabling an achievable pixel size of 1.56 μm × 1.56 μm. The higher resolution images enabled subtle morphological structures to be observed in breast cancer tissue including blood vessels, blood cells, myoepithelial cells, intralobular stroma, and individual terminal ductal lobular units. Fig. 4 demonstrates the enhanced spatial resolution achievable over conventional transmission FTIR microscopic imaging observed by Walsh[55] for imaging colon tissue. Intimate contact is required between the ATR crystal and the tissue, and the technique is therefore generally limited to looking at single regions of interest rather than mapping larger areas. Although no visible tissue damage occurring during the study, the likelihood of subtle morphological and architectural changes due to the presence of the ATR crystal are a potential disadvantage.

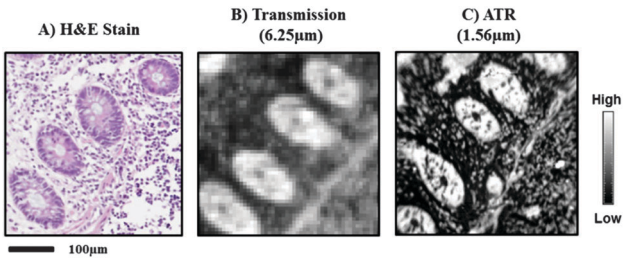

Fig. 4 (A) H&E stain of a colon tissue section showing four colon crypts with an adjacent section imaged using (B) transmission-mode IR imaging (6.25 μm × 6.25 μm) and (C) ATR-mode IR imaging (1.56 μm × 1.56 μm). In both (B) and (C), the peak absorbance of the CH_2 asymmetric vibrational mode band at 2924 cm^{-1} is plotted.[55] Reprinted with permission from M. J. Walsh, D. Mayerich, A. Kajdacsy-Balla and R. Bhargava, High-resolution mid-infrared imaging for disease diagnosis, *Proc. SPIE 8219, Biomedical Vibrational Spectroscopy V: Advances in Research and Industry*, 2012, 82190R–82199R.

Diffraction limited spatial resolution on an FPA system could potentially be achievable by reducing the field of view, and therefore projecting a smaller area of the image onto each detector element. Conventional thermal sources do not generally have sufficiently high intensity for this approach resulting in poor signal to noise and requiring significantly longer collection times. The earliest studies coupling synchrotron radiation to an infrared microscope had demonstrated high resolution images with high signal to noise ratios could be routinely obtained.[56] Single point spectra were a severe limitation of SR FTIR imaging, making it unsuitable for imaging large areas of tissue unless a larger field of view could be used. Coupling FPAs to synchrotrons was initially thought[22] to yield little advantage since the beam would have to be defocussed to fill the full FPA (thus reducing the original brightness of SR) however, Moss *et al.* based at the ANKA synchrotron achieved some success by partially filling a 64 × 64 FPA and concluded that this was the way forward for SR imaging.[57] Hirschmugl[58] utilised a novel approach to integrate the high brightness of a synchrotron source with an FPA infrared microscope at the Synchrotron Radiation Center, Wisconsin USA. The IRENI (Infrared Environmental Imaging) beamline uses an array of torroidal mirrors to recombine 12 extracted synchrotron radiation beams to homogeneously illuminate a sample area of 35 μm × 35 μm. Projecting the beam onto a 64 × 64 FPA resulted in a detector pixel size 0.54 μm × 0.54 μm. This novel approach avoids the problem of having to spread a single beam over a large area. Oversampling enabled spatial resolution at the diffraction limit for all measureable wavelengths, with high signal to noise and short acquisition times. The pixel size obtained is small enough to make infrared chemical imaging competitive with brightfield optical microscopy. In a study by Nasse[59] SR FTIR imaging was compared to conventional infrared microscopy using a thermal source. High resolution images using the high brightness of the synchrotron enabled subtle features such as lymphocytes (diameter 2–7 μm) to be discerned (Fig. 5). The same features could be visualised on the H&E stained section, but not on the image obtained using conventional infrared microscopy. Little or no spectral mixing was observed at boundaries between tissue, and intralobular stroma and epithelium could be clearly discerned. Nasse was also able to identify the basement membrane between epithelium and stroma, a region critical for the early diagnosis of prostate cancer.

Liao[60] also used SR FTIR imaging for investigating amyloid plaques in transgenic mice and Alzheimer diseased brain. High resolution images obtained revealed that the plaques were surrounded by lipid membranes which infiltrated the dense core plaques. More recently synchrotron FPA imaging has been modified[61] and improved using a simplified optical arrangement to split and recombine four beams. Diffraction limited resolution (0.54 μm × 0.54 μm pixel size) enabled high quality images to be recorded of mouse spinal cord tissue with SNR comparable to low resolution images (6.25 μm) taken with a thermal source. A consideration for imaging tissue with SR FTIR is the limited field of view required to get high resolution images. Although highly promising for interrogating regions of

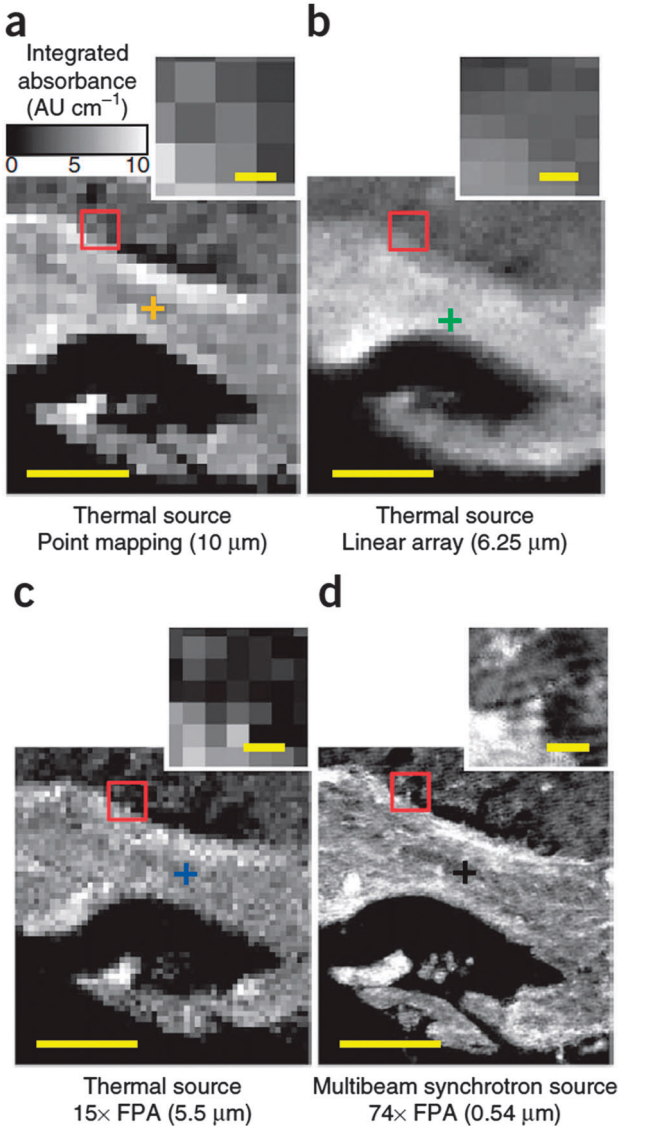

Fig. 5 Chemical images based on the integrated intensity of 2800–3000 cm^{-1} of prostate cancer tissue sections for (a) thermal source point mapping, (b) thermal source linear array, (c) thermal source FPA, and (d) multibeam synchrotron source with FPA. Adapted by permission from Macmillan Publishers Ltd: M. J. Nasse, M. J. Walsh, E. C. Mattson, R. Reininger, A. Kajdacsy-Balla, V. Macias, R. Bhargava and C. J. Hirschmugl, *Nat. Methods*, **8**, 413–416, copyright (2011).[59]

interest on biomedical samples, imaging entire tissue sections requires mapping in a stepwise manner. Needle core tissue biopsies typically have a 1 mm diameter and can be imaged in under 15 minutes with a state of the art lab system utilising a 128 × 128 FPA with a pixel size of 5.5 μm.[62] With a modified data collection protocol and utilising a 128 × 128 FPA this can be reduced further to less than 2 min.[63] Corresponding measurements with an SR FTIR system, even utilising limited numbers of scans per tile would take several hours. Consequently to date the majority of studies have focussed on cells[64–71] rather than large areas of tissue. SR FTIR imaging shows promise in enabling diffraction limited chemical images, but remains a research tool rather than a complementary method for disease diagnosis. Clinical translation requires a laboratory based technique with an implementable methodology to enable it to align with current protocols in the clinic.

The pioneering work at IRENI created a renewed interest in obtaining high resolution images with conventional FTIR microscopes. The advantages of oversampling and recording images with pixel sizes smaller than the diffraction limit were undeniable. Images of unprecedented clarity and contrast could be obtained with the promise of improved disease diagnosis capability. Despite this the understanding of the optimal microscope operating parameters and how these affected image quality was limited. Extensive theoretical models[72,73] of mid-infrared absorption spectroscopy had enabled a thorough understanding of the absorption process occurring with homogeneous and heterogeneous samples. Reddy *et al.*[74,75] built on and extended these models to investigate the optimum operating characteristics for best image quality. Surprisingly the optimal pixel size (1.1 μm) was significantly smaller than being used in most commercial infrared microscopes. The simulations revealed that higher quality images could be obtained using a Schwartzchild objective with a larger numerical aperture and reducing the pixel size to 1.1 μm. Modifying an existing FTIR microscope with a ×74 0.65 NA objective enabled high definition (HD FTIR) images to be obtained, although this resulted in a six to eightfold decrease in signal. HD FTIR applied to colon tissue[55] enabled identification of components and structure which would not be possible using conventional FTIR imaging. High resolution images (Fig. 6) enabled lymphocytes and intracellular mucin to be discerned, both key components in disease diagnosis.

One of the limitations in HD FTIR is the increased measurement time compared to conventional FTIR imaging for a given area. Increased magnification results in a smaller field of view, therefore more infrared tiles have to be collected to image the same area. Furthermore higher magnification spreads the light over a larger number of pixels, reducing signal to noise often requiring longer collection times for a given tile. A recent study by Leslie[62] demonstrated the implications on using HD FTIR chemical imaging for measuring tissue. Utilising a ×35.9 0.65 NA objective enabled high quality images to be acquired with a nominal pixel size of just 1.11 μm. Projection of the image onto a 128 × 128 FPA resulted in an infrared tile of dimensions 142 μm × 142 μm. According to the authors, imaging a single 1 mm breast cancer TMA core required 100 individual tiles to encompass the image, resulting in a six hour collection time. Low resolution images of the core (5.5 μm pixel size) were collected in just 15 minutes. While the image quality and contrast was significantly higher enabling the distinction between myoepithelial and luminal epithelial cells, the increased collection time becomes a limiting factor. Two approaches were suggested in the paper for improving the reduced signal to noise in HD FTIR. Increasing the number of images collected and then co-adding each image (which ultimately increases collection duration), or utilising noise reduction algorithms. Minimum noise fraction (MNF)[76] used in the study not only improved the

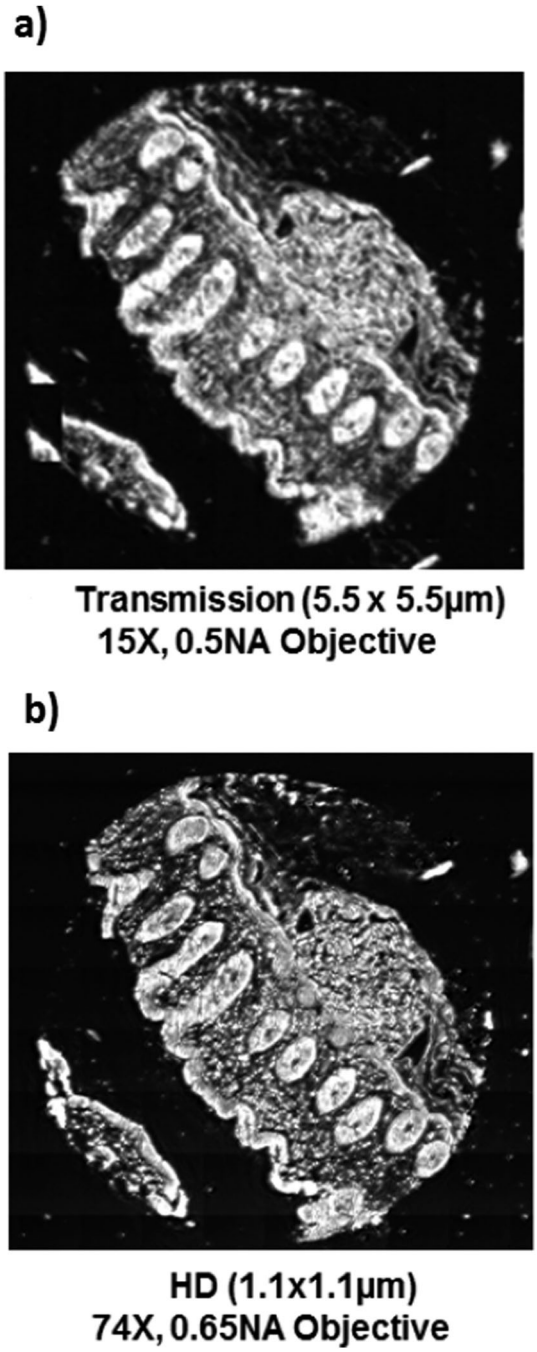

Fig. 6 (a) Low resolution transmission mode with 15×, 0.5 NA objective and (b), high definition mode with 74×, 0.65 NA objective. Lymphocytes and intracellular mucin can be discerned in the high definition image. Reprinted with permission from M. J. Walsh, D. Mayerich, A. Kajdacsy-Balla and R. Bhargava, High-resolution mid-infrared imaging for disease diagnosis, *Proc. SPIE 8219, Biomedical Vibrational Spectroscopy V: Advances in Research and Industry*, 2012, 82190R–82199R.

high definition chemical image, but significantly improved the quality of the spectra, with signal to noise similar to low spatial resolution measurements. Findlay[77] utilised a commercially available novel magnification enhancement optic for performing rapid biochemical imaging at 1.1 µm resolution. Coupling high numerical aperture optics to magnification optics placed

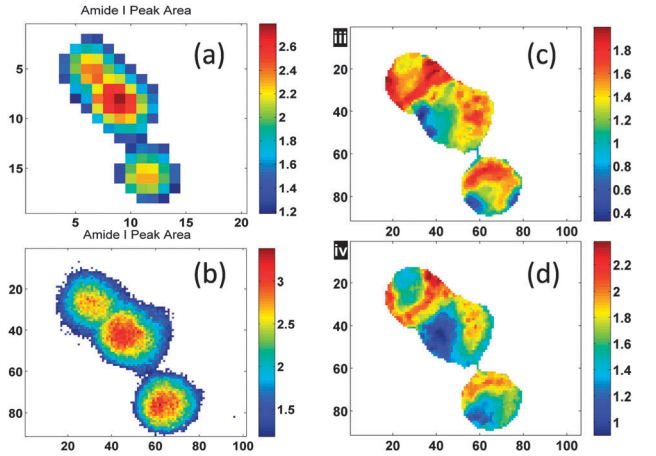

Fig. 7 Shows an infrared image of three fibroblast cells taken (a) at 5.5 µm and (b) 1.1 µm pixel resolution. Images of the amide I and C–H stretching band intensities corrected for scattering and corrected for sample thickness are shown in (c) and (d).[78] Reproduced from ref. 78 with permission from The Royal Society of Chemistry.

immediately prior to the FPA enabled spectra to be collected with high signal to noise ratios.

Infrared images 140 µm × 140 µm could be collected in approximately 6 minutes with signal to noise for the same measurement time comparable to conventional FTIR imaging. Hughes demonstrated how the use of a similar optical system in conjunction with scatter correction and noise reduction could be applied to the study of different types of cells (Fig. 7), namely renal carcinoma cells and human skin fibroblasts.[78] Nevertheless it is currently difficult to envisage HD FTIR being used for imaging a high throughput of tissue due to excessive measurement time. A more practical approach would be to utilise the high throughput advantage of conventional FTIR imaging, and to use HD FTIR as a secondary technique for interrogating regions of interest.

Further improvements in spatial resolution can only really be achieved using tip based spectroscopic techniques where the resolution is determined predominantly by the tip radius, which can be of the order of 50 nm. Photo-thermal techniques using thermocouple tip detectors were pioneered by Hammiche *et al.*[79,80] but this method has largely been superseded by the AFM-IR technique developed by Dazzi *et al.*[81] This latter technique uses an oscillating AFM tip to measure the thermal expansion of the sample when excited by a pulsed IR beam (see Fig. 8). It has been shown that the local spectrum obtained is directly related to the imaginary part of the refractive index and is thus equivalent to the normal absorption spectrum obtained from a conventional transmission experiment, but without interference from scattering artefacts.[82]

Initially the excitation source was the CLIO free electron laser in France but a bench-top system was developed using a lab based laser.[84] It has since been improved further with the use of quantum cascade lasers[85] and the development of resonance AFM-IR in which the pulsed laser source impinges directly on the top side of the sample at the tip location and the pulse frequency is tuned to the resonance frequency of

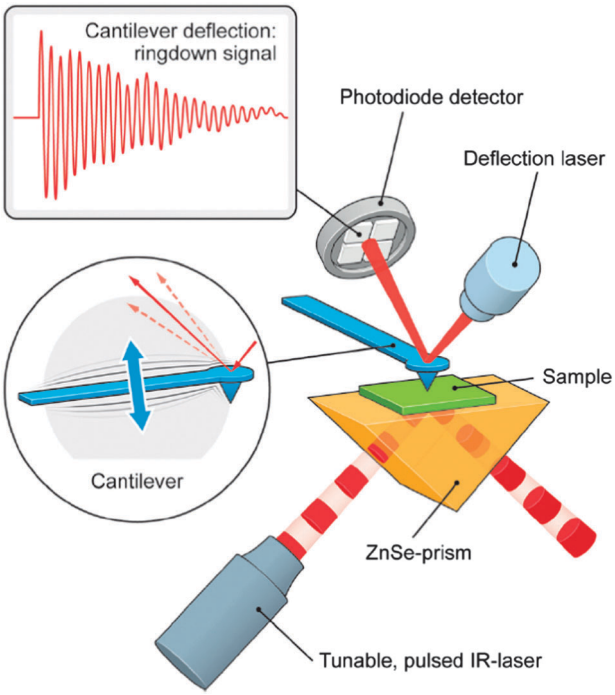

Fig. 8 Scheme depicting the principle of the AFM-IR technique. The sample is deposited on the ZnSe prism and illuminated by a tunable pulsed laser. The probe consists of a standard AFM-lever and detection system.[83] Reproduced from ref. 83 with permission from The Royal Society of Chemistry.

the cantilever. This arrangement enhances the signal measured by approximately one order of magnitude compared with the original illumination though a prism.[86] These systems are now commercially available from Anasys instruments. The non-resonant AFM-IR technique is particularly suited to thin samples with an optimal thickness of a few hundred μm since the photothermal wave expands as it propagates to the surface. For the resonant, top illuminated, method the thickness of the sample is not an issue but it should be remembered that the observed signal is predominantly coming from the top few hundred μm of the surface. These methods appear to have widest application in the polymer and pharmaceutical industries where there is keen interest in chemical information on the nanometre scale.[87] A competitive technique is scattering Scanning Near-field Optical Microscopy sSNOM which has been developed by the Hillenbrand group.[88] In sSNOM, the sharp tip acts as an infrared antenna, focussing the infrared light at the apex thus localising the intense field to the nanoscale region just beneath the tip.[89,90] Collecting and measuring the tip-scattered light thus yields nanoscale-resolved infrared images. Recent developments have seen both QCLs,[91] synchrotrons[92] and free electron lasers[93] used successfully as the excitation source. These near field techniques are currently developing rapidly and warrant a separate review of their own. In this current review we will concentrate on far field IR imaging techniques with an emphasis on disease diagnostics and as such the tip based methods are not considered in any more detail here.

Substrate choice

While spectral histopathology is becoming highly promising for improved clinical diagnosis, several practical barriers currently exist, and these need to be addressed before successful implementation in the clinic. A key question is to establish how infrared SHP would fit into the current workflow. The issue of substrate choice has recently dominated discussions on the practical application of SHP.[94–100] Broadly speaking there are two principal modes of infrared microscopy, commonly referred to as transmission or transflection (see Fig. 2).

In transmission mode tissue is sectioned on to a substrate which is transparent in the infrared region of the electromagnetic spectrum. Calcium fluoride or barium fluoride are commonly used because they are highly infrared transparent but also have the advantage that they are visually transparent enabling staining and visualisation by optical microscopy. However it is currently common practice to stain a serial tissue section on glass, rather than the alkali halide substrate (most likely due to costs considerations), which introduces difficulties in registering the infrared and H&E stained visible images. CaF_2 and BaF_2 slides also have the disadvantage that they are expensive and their fragility means extreme care must be exercised when handling them, making them generally unsuitable for use in automated tissue preparation equipment. In the transflection mode of operation, tissue is mounted onto an infrared reflective substrate, which is generally a glass slide with an infrared reflective coating. The coating can be any infrared reflective material, although commercially available low e-slides (Kevley) consisting of predominantly a tin oxide film with a buried silver layer on glass are commonly used because these are highly transparent to visible light.[101] Infrared light passes through the tissue, reflects from the reflective coating and is then transmitted through the tissue a second time, effectively doubling the pathlength through the sample. Transflection slides have the advantage that they are robust, cheap, and the increased pathlength ensures infrared spectra can be obtained with high signal to noise ratios. Furthermore the tissue sections can be stained post infrared imaging enabling pathological assessment using visible microscopy, enabling excellent registration between the chemical and visible image.

Recently, however, doubts have been raised concerning the suitability of the transflection geometry for biomedical studies. The cause of the concern originates from spectral distortions emanating from the so called electric field standing wave (EFSW) effect.[94] Light impinging on a reflective surface at near normal incidence experiences a phase change of approximately 180 degrees upon reflection.[102] Interaction of the incident and reflected rays results in the formation of a sinusoidal electric field perpendicular to the surface. Since the intensity of an infrared absorption band depends on the square of the electric field, significant variations in absorption intensity are observed at different heights away from the reflective surface. The electric field standing wave effect results in deviations from Beer–Lambert absorption causing spectral distortions which are wavelength dependant. Brooke[95] observed these distortions

when investigating multilayer polymer spheres in transflection mode and found that absorption band intensity did not scale linearly with the thickness of the films. In addition the deviation from the Beer–Lambert law was wavelength dependant. Brooke identified that the variation could be approximated by a squared sinusoidal function further suggesting that the EFSW effect was present. This was supported in work by Filik *et al.*, who showed that there was significant non-linear Beer Lambert absorption using reflective slides.

Recent discussions have focussed on the implications of the EFSW effect, and considered if the effect is profound enough to confound SHP in the transflection sampling modality. Bassan[96] simulated a model multilayer system using Fresnel's equations, of a hypothetical absorber of thicknesses between 0.5–4.5 μm. The data agreed with measured experimental data of cytosine films, (Fig. 9). The spectra clearly show that as the deposited film gets thicker, rather than all bands increasing with the same relative intensity, the intensity of the peaks at the high wavenumber end is initially high relative to those at low wavenumbers but the latter peaks appear to suddenly increase. Note that the equivalent data for thin films on an transparent CaF_2 slide showed essentially no change on peak ratios as the film gets thicker. Extending the model to theoretical cytosine spectra demonstrated excellent agreement between the observed and predicted spectra proving the model to be effective in understanding the spectral distortions arising for the EFSW effect.

Using the model the authors were able to investigate the implications of different thicknesses of tissue on classification when operating in transflection mode. Training and testing a SVM classifier on the simulated spectra for a 4 μm tissue section resulted in excellent agreement with its corresponding H&E. However misclassification was observed when the thickness deviated by just 0.1 μm, and when the thickness was 3.6 μm the classified image was unrecognisable (Fig. 10). The authors suggesting that since current microtome technology cannot guarantee consistent thickness, care must be exercised when operating in transflection for biomedical applications.

The experimental evidence for the EFSW effect and the spectral distortions observed are undisputed. However there is currently limited understanding of the impact these distortions have on potential biomedical applications. Discussions have been dominated within the biomedical field by the EFSW effect and doubts raised over conclusions which have been reached prior to understanding the existence of the EFSW effect. Several studies have focussed on investigating ways to reduce the distortions arising from the EFSW effect. Wrobel *et al.*[97] suggested that integration over the range of incidence angles, varying degrees of coherence of the source and inhomogeneities in sample thickness, significantly reduce the influence of the

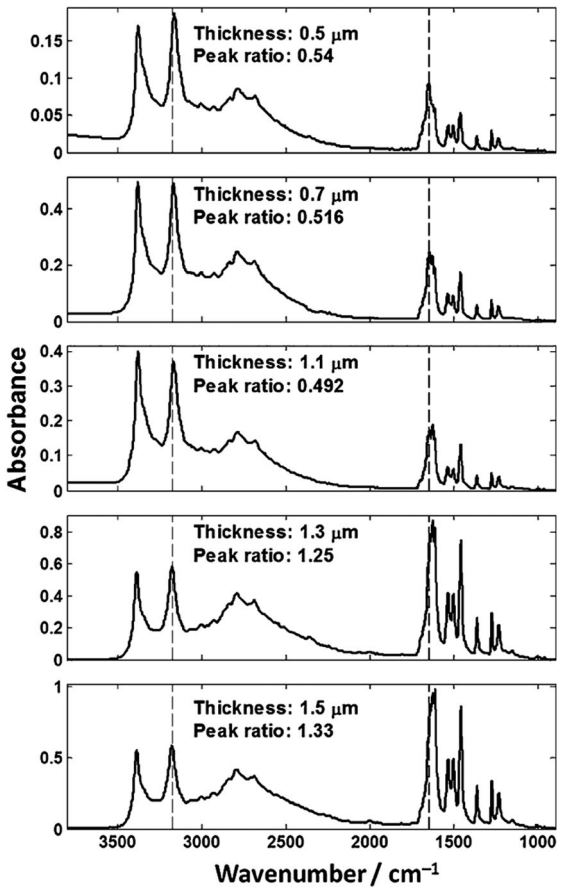

Fig. 9 Infrared spectra of cytosine thin films of various thickness measure in transflection mode. The changing ratio of the 1655 : 3175 absorption bands as a function of thickness clear demonstrates the differing non-linear increase in absorption across the spectral range.[96] Reproduced from ref. 96 with permission from The Royal Society of Chemistry.

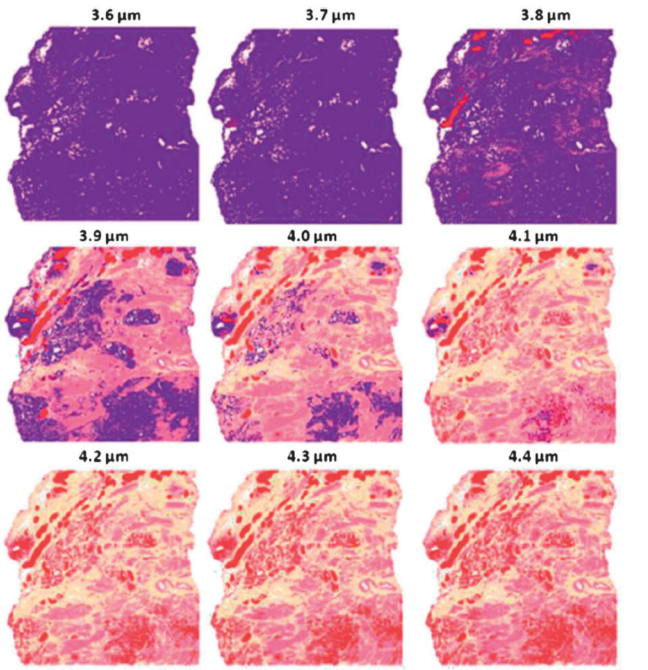

Fig. 10 False colour classification images of the 5 class histological model for prostate tissue. The figure shows the result of a classifier trained on a database of transflection simulated spectra of 4 μm thickness but applied to the same tissue had it been miss-cut over a range of thickness 3.6–4.4 μm. Reproduced from ref. 96 with permission from The Royal Society of Chemistry.

effect on the resultant spectra. It is certainly the case that the Cassegrain collection optics on systems with a high numerical aperture will have a significant angular spread and will thus dampen the relative changes in absorption across the spectral range. The coherence and phase of the source should have little influence on the spectra since in the same way that a pure standing wave (at normal incidence) is unaffected by the phase of the incoming wave, the reflected wave will always be out of phase creating a standing wave meaning that phase does not affect the system. The argument that variations in sample thickness will lead to an averaging of the effect, however, is a spurious one since in imaging the pixels are not averaged. If the tissue in pixels A and B are chemical identical but at different locations and therefore different heights above the reflecting surface, their respective band positions will be different and may therefore be classified as different. They will not be averaged out.

Miljkovic[98] argued that although distortions to the spectra were noticeable in the transflection sampling modality, careful pre-processing could alleviate spurious effects to such a level that they would not create a major problem for SHP. To demonstrate this an infrared chemical image (4 mm × 4 mm) was obtained of fixed cells deposited on to a low-e (transflection) slide. Utilising an extensive pre-processing protocol involving several steps including noise reduction, water vapour reduction, second derivatives and scatter correction enabled spectral distortions to be reduced. Applying a simpler pre-processing regime to representative spectra of 5 μm tissue sections, involving mean centred, vector normalised, second derivative spectra resulted in good agreement between transmission and transflection spectra (correlation coefficient of 0.999). It is important to note, however, that the study utilised a narrow spectral range, only encompassing the fingerprint region between 900–1800 cm^{-1}. It is important to note that such an approach would not be possible with discrete frequency imaging, which is also susceptible to the EFSW in the transflection sampling modality. Cao[99] *et al.* also used second derivative pre-processing while investigating dried cellular monolayers in transflection and transmission mode. Since variations in sample thicknesses are known to exacerbate spectral distortions, atomic force microscopy (AFM) was used to ensure that that there was no significant variations in thickness of the cell monolayers. Partial least squares discriminant analysis PLS-DA scores plots showed no significant separation between transmission and transflection spectra, from which the authors concluded that the spectra obtained from each sampling modality were highly similar. It is interesting to note, however, that classification of an independent test set using PLS-DA gave poorer results for transflection. Based on two replicates sensitivities were 11% and 34% for transflection, with improved classification in transmission mode (although still poor) with sensitivities of 54% and 43% for each replicate.

Using a similar approach but with tissue rather than cells, Kochan[100] also investigated using second derivatives for reducing spectral distortions. Comparing transmission and transflection substrates for canine liver cancer detection, their methodology focussed on ensuring constant sample thickness by using a single laboratory for micro-toming all tissue samples. We note that while using a single microtome in one lab may reduce the variation, studies have shown that thickness variability between replicate sections are approximately 11% for a rocking microtome and 5% for a rotary microtome and average intrasection variabilities is 7% and 4% respectively.[103] Adjacent sections of paraffin embedded liver tissue of 4 μm and 8 μm thickness were mounted onto MirrIR and CaF_2 slides. The samples were left in wax and then chemical images were obtained of similar regions of the tissues in each sampling modality. Repeat measurements were also obtained on the dewaxed tissue, following paraffin removal with xylene. Unsupervised hierarchical cluster analysis (UHCA) using a spectral range 1350–900 cm^{-1} enabled good separation between cancer and normal tissue both in transmission and transflection mode. Good separation was also reported using PCA for 1350–900 cm^{-1}, with four separate centroids observed corresponding to transmission normal, transmission cancer, transflection normal and transflection cancer. Kochan concluded that in this study when utilising a narrow spectral range the spectral features that change for cancer are more significant than those that change due to physical effects such as EFSW. The majority of studies investigating the EFSW effect were qualitative in nature directed at showing differences (or lack of) between each sampling modality. In our own laboratory we have quantitatively investigated the variability in normalised epithelium absorption band intensity from prostate tissue obtained from five separate patients.[104] The tissue sections were obtained from transurethral resection of the prostate from three patients diagnosed with benign prostatic hyperplasia and two with prostate cancer. 4 μm serial sections of prostate tissue were mounted on MirrIR and CaF_2 slides for transflection and transmission measurements respectively.

A database was created from the chemical images consisting of 1900 randomly selected epithelium spectra from each patient. Quantitative information related to band variability in each sampling modality was obtained by considering two separate absorption bands at opposite end of the infrared spectrum. Absorption intensity histograms obtained in transmission revealed a narrow Gaussian distribution (red curve, Fig. 11) showing that for each patient the absorption band intensities were similar, and also that the there was good reproducibility between patients. Histograms plotted from the transflection measurements (blue curve Fig. 11) were significantly broader, and the absorption band maxima varied between patients.

Currently there is still ongoing debate on the impact of the EFSW effect and whether it will have a confounding effect if transflection slides are implemented in biomedical applications. While practical considerations such as cost and robustness make transflection slides highly attractive, the effect of spectral distortions on classification are not fully understood. More research is required in this area using large patient numbers to establish if the transflection sampling modality is fit for purpose.[14]

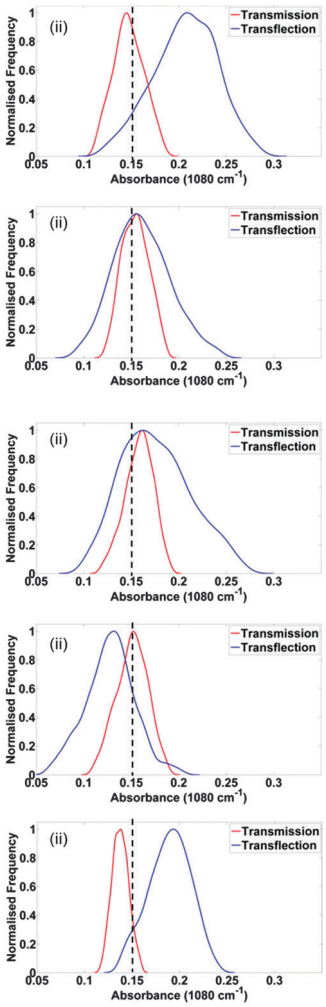

Fig. 11 Distributions of absorbances obtained from 1900 epithelium spectra at 1080 cm^{-1}. The spectra were obtained from adjacent serial prostate tissue sections from 5 patients. The serial sections were mounted either on a 1 mm thick CaF_2 slide or a low-e reflective slide for transmission (red curve) or transflection (blue curve) respectively. The dashed vertical line represents the approximate midpoint of the peak intensity for both sampling modalities. Reproduced from ref. 104 with permission from The Royal Society of Chemistry.

Scattering

While questions still remain on the optimum sampling modality and the suitability of the transflection mode of operation, significant advances have been made on the understanding of how infrared radiation interacts with biological material. For many years the clinical translation of SHP for disease diagnosis had been hindered by scattering effects observed in the infrared spectra of biological materials. The size of cells and sub cellular entities makes them ideal candidates to cause scattering of infrared light. Cells typically range between 8–30 μm in size, and organelles between 1–10 μm. Given that the wavelengths utilised in infrared spectroscopy are between 2.5–10 μm, biological cells are ideally suited to cause intense scattering. Early infrared microscopy studies of eukaryotic cells[105] revealed that it was possible to determine the phase of the cell cycle using spectral differences. However it became apparent that the effects of scattering had not been considered, and that spectral differences could be due to changes in cell morphology as well as biochemical differences. Given that the size and shape of a cell depends on the phase of the cell cycle, it is likely that scattering intensity will change during progression through the cycle.[106–108] Romeo[109] observed large spectral variations in divisionally inactive exfoliated epithelial cells, which should have been generally homogeneous and explained the variability as being predominantly due to Mie scattering. The most obvious effects of Mie scattering is observed as an undulating baseline in infrared spectra of biological material. A sharp decrease in absorption at 1700 cm^{-1}, often referred to as the 'dispersion artefact' also results in a derivative-like lineshape. These effects combined cause variations in relative peak intensity, particularly the amide I and amide II bands which are commonly used for identifying protein secondary structure. Furthermore Mie scattering also results in shifts in the observed frequency of spectral bands, which introduces doubt on conclusions drawn from these highly distorted spectra. Since tissue is composed of cells of various sizes and shapes these distortions are also observed in spectral histopathology, particularly at the edges of tissue architecture. This is a particular problem for highly glandular tissue such as prostate or sponge like tissue such as lung where a high percentage of the sample consists of the edges of holes. In the case of prostate, the situation is exacerbated since the epithelial cells that become cancerous (and are therefore of most interest) are secretary cells (designed to secrete fluid into the "holes" and are by design at the edges) thus suffer from the most severe spectral distortion. Clearly for the implementation of SHP for disease diagnosis in the clinic, spectra in the absence of scattering need to be obtained either by practical means or by scattering correction algorithms. While it is possible to correct the undulating baseline using a rubber band base line correction, this has no effect on the variations in peak position caused by Mie scattering. Kohler[110] utilised a modified extended multiplicative scattering correction (EMSC), by estimating a large number of Mie scattering curves based on a range of possible particle sizes and refractive indices. While the corrected spectra had the undulation removed and much improved baselines, the 'dispersion artefact' remained meaning that the variations in peak positions and intensity were uncorrected. Correcting for the dispersion artefact required a more thorough understanding of its cause to be developed.

The complex biochemical structure of cells and tissue make it difficult to understand the scattering mechanism and how this causes the observed spectral distortions. Bassan[111] utilised polymethyl methacrylate (PMMA) micro spheres as a simplified model to investigate scattering effects in cells. Since the spheres were known to be homogeneous and of accurately known sizes this enabled scattering effects to be investigated in the absence of chemical effects.

Having understood the cause of spectral distortions in biological material it then became necessary to investigate ways to correct for Mie scattering. The first resonant Mie scattering correction algorithm is based on van de Hulst's[112] approximation

to full Mie theory. The RMies correction algorithm proposed by Bassan[113] extends on EMSC theory by introducing a fourth term, which accounts for the resonant Mie scattering in addition to the multiplicative effects. The RMies correction algorithm has also been extended to utilise full Mie theory,[114] which was demonstrated to produce similar results to the algorithm using the van de Hulst approximation, for PC-3 cells but is considerably more intensive computationally. More recently the RMies correction algorithm has been applied to biological tissue samples rather than spectra obtained from single cells.

Fig. 12(a) and (c) show total absorbance (area under each spectrum) FTIR images of prostate tissue from two different patients patient 1 and 2. The colour scheme is and infrared heat-map such that white indicates high absorbance. Fig. 12(b) and (d) show fluorescence images of prostate tissue from the adjacent serial section to Fig. 12(a) and (c) respectively, which have been stained with anti pan cytokeratin antibody. This antibody stains for prostate epithelial cells and these are indicated by the green pixels. As mentioned previously the epithelial cells make up the edge of the lumen (hole in the tissue) and therefore suffer from severe distortion. This is indicated in Fig. 12 (bottom panel (a)) where the spectrum has a severely distorted baseline and a significant shift in the position of the amide I band. A rubber band correction of this spectrum would flatten the baseline but leave the amide I band position uncorrected. The RMieS-EMSC corrected spectrum is show in Fig. 12 (bottom panel (b)). As can be seen the amide I ban had shifted to higher wavenumber.

Bamberry[115] evaluated the performance of the RMies-EMSC using FTIR FPA chemical images obtained from tissue sections obtained from human cervical transformation zone and Wistar rat brain. Prior to imaging, the formalin fixed paraffin embedded 4 μm sections were mounted on to MirrIR slides and dewaxed with xylene. Dewaxing is known to exacerbate Mie scattering from tissue, since it removes the refractive index matching present in paraffin embedded tissue. The transflection sampling modality[116] has been demonstrated to contribute to the 'dispersion artefact', and increase spectral distortions. It was found that although using just a single iteration of the RMies correction algorithm produced reasonable quality chemical images, the spectra were over corrected and retained some of the features present in the Matrigel reference spectrum. Utilising eight iterations, although time consuming, enabled corrected spectra to be obtained with improved correspondence to the absorption bands in the original data, and the spectra also had improved baselines. Furthermore using an average spectrum from the sample set as the reference spectrum instead of the built in Matrigel reference also improved the correction. Unsupervised hierarchical cluster analysis of the uncorrected and corrected FTIR data showed good agreement between each other and to the H&E stained section. However the RMies corrected unsupervised hierarchical cluster analysis (UHCA) image showed improved differentiation of the exfoliating cell layer, superficial squamous epithelium, intermediate layer and parabasal layer. Interestingly in the corrected image the stroma was described using two clusters while in the uncorrected image this increased to three. The authors commented that since stroma is relatively homogeneous, describing it with fewer clusters confirms an improved result using the correction algorithm. However it was

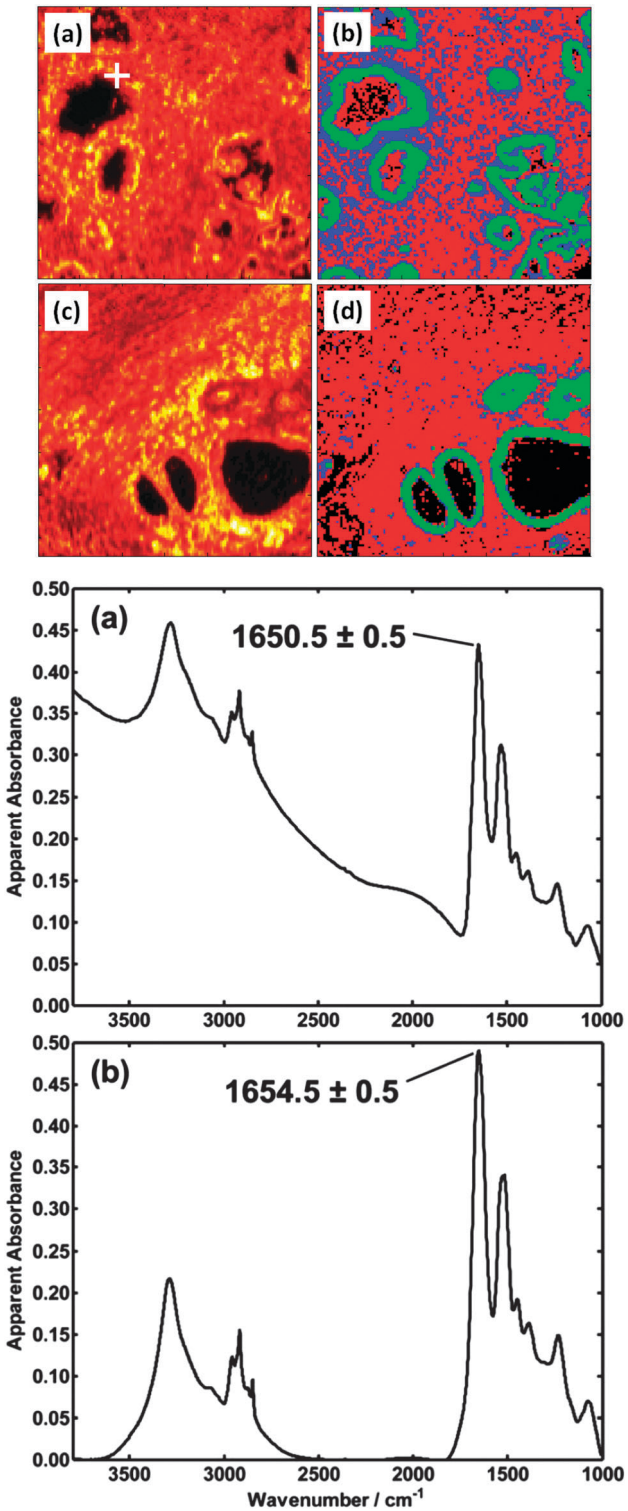

Fig. 12 (top) Infrared absorbance image of prostate tissue (a) and (c) and the corresponding anti pan cytokeratin antibody stained tissue (b) and (d) indicating the location of epithelial cells. Bottom (a) a raw infrared spectrum from epithelial cell, (b) RMieS_EMSC corrected spectrum. Reproduced from ref. 117 with permission from The Royal Society of Chemistry.

found that to produce the best results the algorithm had to be used iteratively. Given the large dataset used in the study (65 536 and 16 384 spectra for the cervical tissue and rat brain respectively), and that parallel processing was not used this impacted on processing times. The cervical tissue and rat brain took 53 hours and 10 hours respectively to process. One study[117] has investigated the optimum number of iterations of the RMies correction algorithm, to determine how this affects histological classification. Prostate tissue sections from two patients were stained with anti pan cytokaratin to identify areas of epithelium (green) and stroma (red). Overlaying the stained image with the FTIR image for patient 1 enabled areas of epithelium and stroma to be identified, and this was used to train an artificial neural networks classifier (ANN). The trained ANN classifier was then used to classify patient 2 on spectra which had been RMies corrected using 5, 10, 20 and 30 iterations. By comparison to the stained image it was observed that reasonable classification is achieved after just 5 iterations, although significant improvements in the classification are obtained using 10 iterations. The authors note that 20 iterations would have taken approximately 8 days if a single computer was doing the processing, however in this study high throughput computing utilising parallel processing reduced the processing time down to approximately twenty minutes. However, since tissue biopsy samples are likely to encompass a larger area than used in this study this is likely to impact on processing times. Even using high throughput computing performing the RMies correction on a single biopsy core is likely to take several hours.

Miljkovi *et al.*[98,118] have developed a much faster method of correction in which distortions in the observed spectra, are removed by phase correction between the real and imaginary components obtained by finite Hilbert transform (truncated reverse FFT) of the observed spectrum. This is much faster than the RMieS-EMSC correction and takes out the dominating reflection component very well.

Dewaxing

Implementation of SHP requires a method which is fast and reliable. The lengthy processing times for the resonant Mie correction are not practical and serves as another barrier to clinical translation. An alternative to correcting for scattering computationally is to minimise scattering experimentally. Dazzi[119] demonstrated that it is possible to minimise contributions from scattering using an integration sphere coupled to an off axis DLaTGS (deuterated L-alanine doped triglycerine sulphate) detector. PMMA spheres of varying diameters were used to vary the amount of Mie scattering. In transmission mode using spheres larger than 0.62 μm resulted in the spectra became highly distorted due to Mie scattering. Spectra obtained using the integrating sphere appeared similar to a thin film of PMMA, demonstrating that the scattering distortions had been significantly reduced. However it is difficult to envisage how an integrating sphere could be coupled to an FTIR imaging system using an FPA detector. Another possible solution is to leave the tissue in paraffin rather than dewaxing. This has the advantage that there is good refractive index matching between the tissue and the paraffin which can significantly reduce Mie scattering, particularly in highly glandular tissue such as prostate. Therefore it becomes possible to use the considerably faster non-resonant Mie correction algorithm,[39] or use a manual linear baseline correction.[63] Just as importantly, given that the tissue is often a valuable and scarce resource, leaving the sample in wax has the added benefit that the tissue remains preserved and can be reanalysed at any time by the same or indeed other analytical techniques. Paraffin wax has intense absorption bands at 1462, 2846, 2920 and 2954 cm^{-1} which overlaps with the lipid region and can obscure important tissue vibrational bands. Whether to deparaffinise samples or not is still a matter of some debate and commonly discussed within the biomedical field. Doubts have been raised as to the effect the dewaxing process has on human tissue, and indeed whether the sample has been fully dewaxed. The situation is complicated by the overlap of paraffin bands with the lipid bands, therefore even in a well dewaxed sample the paraffin bands will not disappear. Detailed studies have been performed on the dewaxing process using different solvents and immersion durations. In a time resolved study by Hughes[120] it was shown that when using either xylene or hexane as the solvent, no further significant changes are observed in the transmission infrared spectra after a period of ten minutes.

It was further suggested that solvent resistant lipids remained in the tissue, and that extended solvent exposure would be unlikely to cause these bound lipids to leach into the solvent.

Some progress has been made in using algorithms to digitally dewax infrared spectra acquired on paraffin embedded samples. Digital methods have the advantage of eliminating the use of expensive and hazardous solvents, and removes the risk of harsh chemicals affecting the integrity of the sample. Furthermore it removes the risk of incomplete dewaxing which is present with chemical methods. However removal of the paraffin signature from a tissue spectrum is not trivial due to variations in sample thickness. Furthermore differing protocols are likely to exist between laboratories for the formalin fixation and paraffin embedding process, which can produce variability in the paraffin spectra. One approach is to acquire infrared spectra from a series of different paraffin samples. PCA has been used previously by Ly[121] to maintain the maximum variance of the paraffin spectra. Extended Multiplicative Signal Correction was then used to correct for the spectral signature of paraffin. K-means clustering following the correction for the range 900–1800 cm^{-1} produced a different spatial distribution than when using the paraffin free region of 1350–1800 cm^{-1}. The authors suggest that this could be due to potentially meaningful biochemical information located within the paraffin region. They have since used this digital dewaxing methodology in a number of other studies on a number of different tissue types.[44,122,123] Nguyen[124] has recently investigated skin collagen orientation with aging with polarised FTIR imaging for paraffin embedded samples. Pre-processing with

EMSC neutralised the paraffin signal, and also enabled the removal of outliers and tissue with poor signal to noise ratio. Pre-processing with EMSC was important in the study since collagen contains infrared absorption bands which overlap with those of paraffin. HCA applied to infrared images corresponding to the dermis revealed that for younger skin the collagen fibres are oriented perpendicular to the skin surface, and as skin ages they become parallel to the skin surface. While EMSC effectively neutralises the paraffin signal through ensuring the paraffin bands have the same intensity in each spectrum, it does not remove them. Gobinet[125] developed a method for the removal of paraffin bands from Raman spectra of paraffin embedded human skin biopsies using a combination of Independent Component Analysis (ICA) and Non negatively Constrained Least Squares (NCLS). ICA estimates the paraffin spectrum from the acquired image, and then NCLS is used to estimate the 'concentration' of the paraffin spectrum to be subtracted from each spectrum. The method has subsequently been applied to FTIR spectra obtained from formalin fixed paraffin embedded samples of skin carcinoma.[126]

Cryofixation for the long term storage of tissue samples is becoming increasingly popular within the SHP community. Freezing samples removes the need for chemical fixatives and therefore alleviates any risk of the tissue being chemically modified. Furthermore the absence of paraffin in the samples means the lipid region becomes available allowing access to all potential biomarkers. Liao *et al.*[60] have utilised frozen tissue for investigating amyloid plaques in transgenic mouse brain. Lipid membrane-like signatures were observed which penetrated to the core of the plaques. Hackett[127] has compared cryofixed and formalin fixed murine brain tissue using FTIR imaging and proton induced X-ray emission spectroscopy (PIXE). Differences in peak areas were observed for the second derivative infrared spectra between cryofixed and formalin fixed tissue, suggesting that proteins, phosphates, carbohydrates, and either unsaturated lipids or lipid oxidation products were leaching from the tissue during the formalin fixation process. Furthermore PIXE revealed that the formalin fixation process mobilises Cl^- and K^+, and these ions are leached from the tissue. Hackett concluded that while formalin fixed samples have the potential to be used for discriminating between healthy and diseased tissue, cryofixation is more suitable if the aim is to observe the biochemical changes associated with the diseased state. While using cryofixed tissue is an exciting development in the biomedical field, there are several disadvantages which are likely to hinder clinical translation. Samples need to be stored in a low temperature freezer (-80 °C) and prior to use must be fully thawed and dried, a process which can take several hours and which must occur in a dry, dark environment. In addition, at room temperature the tissue starts to quickly degrade and therefore has to be imaged as soon as possible.

The debate on whether to use cryofixed, formalin fixed paraffin embedded or dewaxed samples (chemically or digitally) is likely to continue, more research needs to be conducted to establish if the presence of wax has an adverse effect on SHP disease diagnosis.

Disease diagnosis through SHP

Despite worldwide improvements in healthcare the number of new cancer cases is increasing yearly. According to the world health organisation (WHO) the number of new cancer cases is expected to increase by 70% over the next two decades.[128] Cancer mortality rates can be reduced by early detection and treatment, and this has led to screening programs aimed at diagnosis before physical symptoms are manifested. Cancer screening (which may involve blood tests, X-rays or smears) are designed to detect abnormalities which could in the future lead to cancer. In cases where abnormalities are detected a biopsy is performed to obtain tissue for pathological assessment. Unfortunately the screening process is designed to have high detection rates for cancer, but this often results in a high level of false positives and therefore a large number of biopsies are unnecessarily taken each year. In the case of breast cancer approximately 1.6 million biopsies are performed each year.[129] Studies[130] have shown that only approximately a quarter of these are diagnosed as cancer, with the remainder being due to either benign or pre-cancerous conditions.

Current histopathology practice is for tissue obtained from biopsies to be formalin fixed and paraffin embedded. Thin layers of tissue (typically in the region of 1–5 μm) are then microtome sectioned and mounted onto glass slides for de-paraffination and staining. Currently no automated screening exists for identifying abnormal tissue in biopsies. Each biopsy needs to be assessed by a highly trained pathologist and a significant amount of time is spent analysing normal samples. The desire for increased throughput has recently led to an increased interest in chemical imaging as a pre-screening tool.

Infrared microscopy has become one of the key techniques in the biomedical field for interrogating tissue. In partnership with multivariate analysis and machine learning techniques, it has been widely accepted as a method which can distinguish between normal and abnormal tissue with both high sensitivity and high specificity. Numerous examples of this exist in the literature and IR chemical imaging has been used to classify prostate,[131–137] brain,[138–141] kidney,[142] lung,[42,43,143] skin,[41,121,144,145] colon,[44,146] breast,[147–149] liver[100,150] and bladder cancer[151,152] and also Alzheimer's disease.[153] In some cases the studies utilised the high spatial resolution available in single point collection mode, measuring isolated regions of interest from a large tissue sample. The time required to acquire the data meant there was a limit on the number of spectra which could be collected and/or the number of patients studied. Obtaining large numbers of spectra from limited numbers of patients often leads to overtraining which can result in poor classifier performance when new patients are added to the database.[154] Despite the studies enabling detection of cancer with high sensitivity and specificity, the limited patient numbers used within some studies[132,140,142,148] prevented proper validation of the results. Intra-class variability is expected to be small and inter-class variability large for data sets encompassing a small number of patients.[155] As more patients are introduced the intra-class variability increases while the inter-class variability

reduces making it more difficult to differentiate between classes, *e.g.* benign *versus* malignant. Large patient numbers in both the training set and independent test set are required for robust models to be build and validated. In a study by Mu[42] on lung cancer tissue biopsies, the effect of the number of patients in the training data set on classifier accuracy on an independent test set has been investigated. Based on ten independent repeat SVM classifications, increasing patient numbers in the training set while maintaining constant numbers of training spectra was observed to improve accuracy and reduce scatter. However the actual number of patients required is difficult to state since it varies significantly depending on the degree of difference between classes but in an excellent paper by Beleites *et al.*[154] entitled "*Sample Size Planning for Classification Models*", which deals specifically with cell and tissue identification, the implication is that 100s of independent samples are required in each class. Unfortunately it is often difficult to obtain such numbers particularly from a single hospital and for rare diseases. Clinical translation of infrared microscopy for SHP requires that large numbers of spectra from large patient cohorts can be collected quickly in an automated manner. Tissue Micro Arrays (TMA's) were originally used for high throughput molecular screening of tumour samples. Utilising 600 μm tissue needle cores biopsies separated by only 0.1 mm, Kononen[156] was able to fix as many as 1000 tissue cores on to a single glass slide. Several advantages have been identified for utilising TMA's for SHP rather than imaging large areas of tissue on separate slides. TMA's have the advantage that spectroscopic measurements on a large number of tissue samples can be obtained at the same time, thereby removing any variation originating from the conditions under which the data was acquired. Variations in sample hydration,[157] temperature and humidity are known to affect reproducibility of spectra, and measuring multiple tissue cores in one cohort enables decoupling of this variability. Tissue harvested from different hospitals are unlikely to use exactly the same work practices for fixing, embedding and sectioning thereby introducing further variability. Incorporating a large number of tissue cores onto a single infrared slide ensures that all samples were prepared under similar conditions. An obvious disadvantage of TMA's is that the area of tissue being analysed is relatively small making pathological assessment difficult in some cases. For example low grade prostate cancers (Gleason score 2–4) are generally small and rarely seen in tissue biopsies and are usually seen in transurethral resections only.[158] Furthermore the absence of abnormal tissue in a single biopsy core does not guarantee the patient is cancer free. Multiple needle core biopsies often need to be taken to ensure the tissue obtained is representative of the surrounding tissue. Despite this the main advantage is the high throughput achievable using multiple needle core biopsies on a single slide. Typically a commercially available TMA will consist of up to 200 1 mm cores, or 600 high density 0.6 mm cores. Utilising current state of the art FPA technology enables a full array to be collected in a matter of hours.

As early as 2005 Fernandez[135] was utilising prostate TMA's for infrared histopathologic class recognition. Despite only using a 16 element linear array detector, meaning that imaging a single core took approximately forty minutes, utilising TMA's still enabled a large spectral database to be constructed. In a large study encompassing 870 individual tissue samples, a subset of 3 million spectra from 262 samples was examined. Focussing on histology this seminal paper demonstrated that ten separate classes of tissue could be clearly differentiated. The study highlighted that by building a classifier based on carefully selected frequencies of interest, and utilising distinguishing spectral features known as metrics, that histological classes could be predicted with sensitivities ranging from 90.09% (nerve) to 99.1% (epithelium). The classifier was also used to classify the histology of entire arrays providing false colour rendered images with good qualitative agreement with the corresponding H&E stained sections. Utilising a two stage process for SHP cancer diagnosis, pixels in the infrared chemical image relating to epithelium were first identified from a set of 50 samples consisting of normal or cancerous tissue from 25 different patients. Epithelial spectra were then classified as either malignant or benign using a classifier operating with a subset of 20 metrics. Although adenocarcinoma was classified in the normal samples, there was a significantly higher classification fraction of adenocarcinoma in the cancerous samples. Setting a 20% threshold for the adenocarcinoma fraction enabled a reported detection of malignancy with 100% sensitivity and 100% specificity.

Despite the key advantages of using TMA's for analysing large patient data sets, throughput was effectively limited by the acquisition time when using linear array detection. Bird[45] investigated the feasibility of using infrared SHP for the classification of different types of lung cancer. Utilising TMA technology consisting of a single slide with 80 biopsy cores enabled a spectral database to be constructed from a large number of patients. Rapid scanning with a 16 element linear array detector enabled 16 pixel spectra to be collected in just 0.85 seconds. Rastering enabled a single 1.5 mm diameter core to be collected and processed in approximately 45 minutes. In one of the largest SHP studies at the time over 3 million spectra were collected from over 70 patients. A data base was constructed consisting of over 100 000 spectra which were annotated as cancerous or normal, and also the type of cancer. Classifying with multilevel artificial neural networks (ANN's) enabled differentiation of normal *versus* abnormal tissue with 99.3% sensitivity and 94.4% specificity. Furthermore the multilevel classifier enabled distinction between different types of lung cancer. Once the first level ANN had classified tissue as cancer, the next level ANN could determine if it was a small cell lung carcinoma or not with 91.2% sensitivity and 98% specificity. The study demonstrated that by using large patient data sets SHP could classify cancer and cancer types with similar accuracy to multipanel immunohistochemistry (IHC).

Bassan[39] demonstrated the high throughput capability of FTIR imaging for looking at large areas of tissue. Utilising an FTIR microscope coupled to a 128 × 128 focal plane array detector a 0.704 × 0.704 mm region could be imaged with 5.5 μm spatial resolution. Bhagarva[20] had previously demonstrated

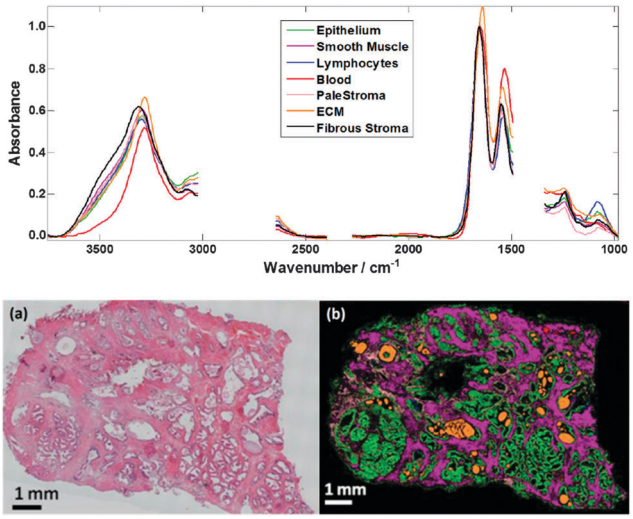

Fig. 13 Top, shows the mean spectrum for each tissue component in the database. Regions of the spectrum have been removed due to paraffin hydrocarbon stretching region *ca.* 2700–3000 cm^{-1}, paraffin hydrocarbon bending vibrations *ca.* 1340–1490 cm^{-1} and the CO_2 absorption *ca.* 2300–2400 cm^{-1}. Bottom, (a) H&E of a prostate tissue specimen and (b) the respective false colour classification image. Colour scheme as follows: epithelium = green, smooth muscle = purple, blood = red, ECM = pale yellow, fibrous stroma = pink, concretion = orange and lymphocytes = blue.[39]

that spectral resolution only impacts on classifier performance if measurements are made at resolutions of or lower than 16 cm^{-1}. In fact classification accuracy only drops off significantly when 32 cm^{-1} spectral resolution is used. Acquiring chemical images at 8 cm^{-1} resolution allowed Bassan[39] to collect a single 0.704 × 0.704 mm infrared tile in just 14.5 seconds. Large tissue areas of approximately 12 mm × 5.5 mm were measured using the mosaic method of collection. The chemical images consisted of 17 × 8 (136) infrared tiles, and were comprised of approximately 2.3 million spectra. Complete tissue sections were collected in just 33 minutes demonstrating the potential of using FPA technology for rapid infrared chemical imaging (Fig. 13). Using a random forest classifier, histological classification of different tissue types was performed on an independent test set with high levels of accuracy (98.02% epithelium, smooth muscle 97.04% and fibrous stroma 98.48%).

High throughput chemical imaging was demonstrated in the study while maintain high levels of accuracy of histological classification. Großerueschkamp[43] has used high throughput chemical imaging for marker free histopathological annotation of lung tumour subtypes. Motivated by Bird's[45] study on lung cancer TMA's the work investigated identifying with SHP five different classes of lung cancer, but also attempted to distinguish between subtypes of adenocarcinoma. Instead of using TMA's large area frozen tissue samples were used for improved pathological annotation. Two instruments were used to collect chemical images of the tissue, the first utilising a 64 × 64 FPA and the second a 128 × 128 FPA detector. The large field of view obtainable with these instruments enabled a large spectral database to be constructed consisting of approximately 15 million spectra from 101 samples (92 patients). Unfortunately acquisition times and the size of the areas of tissue used are not discussed in the paper, nevertheless the study demonstrates that large tissue areas from a substantial patient population can be collected when using high throughput technology. Furthermore this large study showed that excellent classification rates can be achieved using large tissue samples from both cancer types (97%) and cancer subtypes (95%).

Recently Wald[41] investigated primary melanomas using infrared chemical imaging to determine whether infrared signatures could be used to assess the risk of metastasis. Rather than imaging a whole TMA, areas within biopsy cores were selected to encompass where there was a large diversity of cell types. Utilising this approach the study was able to include a diverse and large number of patients. A 64 × 64 FPA detector used in the study enabled a 180 μm × 180 μm area to be imaged with a single infrared tile. The study used 91 areas of measurement from 81 different patients on a TMA consisting of 208 core biopsies. Principal component analysis enabled good separation of 6 different classes of cells (melanoma cells, connective tissue, erythrocytes, necrotic cells, keratinocytes, and lymphocytes) in primary melanomas. Supervised partial least squares discriminant analysis (PLS-DA), correctly classified melanoma cells at a level of accuracy of 98%. No significant differences were observed in the infrared spectra between melanoma cells in primary tumours to melanoma cells in metastases. However spectral differences in melanoma cells in the primary tumours were observed for patients with skin cancer at stage I or stage II and stage III or stage IV. Using external validation PLS_DA was able to predict which group melanoma cells belonged to with 88.9% sensitivity and 70.6% specificity.

Some studies indicate that infrared microscopy can be used to detect modifications to tissue adjacent to cancer. The role of stroma in the progression of cancer is currently an interesting area of investigation. Kumar[159] has used FTIR imaging to investigate the change in the microenvironment of breast cancer. Eight tumours of different grades from eight different patients were imaged with particular focus on (i) the cancer area, (ii) the extra cellular matrix (ECM) close to the cancer, and (iii) the ECM far from the region of cancer (>500 μm). The largest spectral differences between the three regions was identified to be due to the bands at 1630 and 1640 cm^{-1}. For regions close to the tumour the 1630 cm^{-1} band was observed to be more intense than 1640 cm^{-1}, which was tentatively assigned to changes in ECM chemistry due to tumour proximity. Utilising PCA and the ratio of the two bands showed a continuous progression in collagen spectral features when moving away from the tumour, indicating that the ECM may have a role to play when diagnosing cancer using SHP. Several other studies[160,161] have also confirmed that biochemical changes are observed in the tumour microenvironment, *i.e.* within the stroma, and that these changes can be monitored with infrared microscopy. Stroma has also been used recently[137] for predicting incidence of recurrence of prostate cancer. Prediction of clinical outcomes and likely prognosis for the patient are key deliverables when deciding on the best course of treatment for the patient. Poor decision making arising from the only modest success of currently available

tools means that the most common types of cancer (Gleason 7) are not treated effectively. Utilising a large population of 186 patients with mainly mid-grade cancer a Ranking Support Vector Machine was used to attempt to classify those patients which would be recurrent. While epithelial data was unable to discriminate between recurrent and non-recurrent cases, the classifier based on stromal data had a classification accuracy of approximately 70%.

To date the majority of studies have been performed in isolation and there has been limited sample or data sharing to establish if SHP results obtained in one laboratory can be reproduced elsewhere. Furthermore when a classifier is constructed the performance is usually validated using samples which have been measured on exactly the same instrument. Translation into the clinic requires that SHP models can be trained on samples from one clinic and used to predict the disease state of samples obtained elsewhere. Even in the presence of well established protocols it is likely that working practices and operator level of skill will have an impact on how reproducibly tissue samples can be prepared for SHP analysis. Variations in instrumentation are also potential confounding factors since it is difficult to envisage identical spectral platforms being used in every clinic. Variability between identical instruments requires strict protocols being implemented to ensure that instruments are working to specification, particularly important for validation purposes when clinical decisions are being made on the data acquired. Only limited studies have investigated building a model for diagnosing cancer on one instrument and testing it on another. Cross platform variability[162] has been investigated by Ergin to establish if significant differences would be observed when chemical images were acquired on the same instrument type in different laboratories, and for different instrument types in different laboratories. Chemical images were acquired of 1.8 mm diameter lung cancer needle core biopsies in transflection mode. In each case the following pre-processing steps were performed: spatial averaging (pixel binning factor 4) followed by conversion from transmittance to absorbance, vector normalisation, noise reduction using principle component analysis, water vapour reduction using the techniques first proposed by Bruun,[163] correction for resonant Mie scattering and finally quality testing to remove any low signal spectra or those which were from areas of thin or no tissue. The spectra were then truncated to the fingerprint region (1000–1800 cm^{-1}) which contains most of the biologically relevant information. Spectral resolution and spatial resolution were slightly different on the FTIR microscopes from the two different manufacturers. Therefore both the pixel size and data spacing were interpolated to 12.5 μm and 2 cm^{-1} respectively to ensure comparability. It was also necessary to register the images since it is almost impossible to image the same region of tissue in two consecutive measurements. Five separate and independent tests were performed to investigate cross platform transferability.

Consecutive measurements using the same instrument and the same background were found to be highly reproducible. Correlation coefficients of 0.992 and 0.996 demonstrated high reproducibility, indicating that fluctuations in water vapour and in the infrared source or detector had a very limited effect on the acquired data. There was less reproducibility, however, dual centre study involving labs in Germany and the USA. Correlation coefficient reduced to 0.958 and 0.974 when comparing the images obtained on the same sample and on the same instrument type but in different laboratories. The authors suggested that this was potentially due to variations in transflected intensities due to variations in the focussing optics on each instrument. To investigate this, the height of the focal plane was varied for a given instrument. Provided that the focal plane heights were within 5 μm of one another then excellent spectral reproducibility was observed. Using differences in focal plane height of over 5 μm caused the mean correlation coefficient to reduce significantly. The effect of poor focussing was further demonstrated by the authors by tilting the reflective slide with respect to the focal plane. Null spectra obtained by ratioing infrared spectra obtained from the four corners, were observed to be vertically offset from one another instead of having zero absorbance. In the most extreme case the offset had an absorbance of 0.02 which amounts to a change in reflectivity of approximately 5%. The authors concluded that it was the choice of background area, slide reflectivity and focussing which had an impact on reproducibility and that reproducibility between instruments was quite high. These preliminary findings on cross platform transferability are encouraging, and suggest that if carefully constructed protocols can be written for sample measurement then reproducible data can be acquired irrespective of the instrument. Establishing cross platform transferability is likely to require much more extensive data sharing across the biomedical community to ensure that clinical decisions reached are equally valid irrespective of location.

Future directions

Since FTIR microscopy was first used to produce chemical images of tissue there has been a dramatic improvement in data acquisition and processing speeds. However, despite FTIR microscopy with an FPA being able to take several thousand spectra simultaneously, measurements from a tissue micro array (TMA), encompassing several million spectra often takes several hours. The problem lies with the vast quantities of data which FTIR collects, each pixel in a chemical image is derived from a full infrared spectrum itself composed of thousands of individual data points. Data management is quickly becoming a barrier to clinical translation and poses the question of how to store these incessantly growing data sets. Since FTIR collects all wavelengths of infrared light concurrently, reducing the acquired spectral range through undersampling does not reduce collection times. Operating at lower spectral resolution, or co-adding fewer scans can reduce acquisition times but ultimately deteriorates the quality of the data. Recent research[39,63] has raised doubts as to whether the full spectral range is actually required for accurate disease diagnosis using spectral histopathology.

These studies suggest that once spectral biomarkers have been pre-determined it may be possible to diagnose disease based on a limited number of discrete spectral features. Prior to the widespread use of FTIR, dispersive infrared spectrometers were the norm with spectra collected by measuring each wavelength individually and consecutively. Despite having long acquisition times when measuring full spectra, the serial nature of the technology meant narrow spectral ranges could be measured relatively quickly. However limited throughput in dispersive instruments due to the use of gratings and apertures, makes them generally unsuitable for imaging applications. Recently discrete frequency infrared imaging utilising mid-infrared optical filters have been proposed as a viable alternative. Practical application requires that the filters must have high throughput, while still achieving transmission of a narrow spectral range. Furthermore given that a working system needs to be capable of accessing the entire mid infrared region, multiple filters will be required so they must be low cost. Kodali *et al.* have proposed Guided Mode Resonance (GMR) filters as a possible candidate for use in discrete frequency infrared imaging. The operating principle is that at the resonant wavelength the device exhibits high reflectivity over a narrow wavelength range, with high transmission off-resonance. Retro-fitting the devices on a rotating wheel to the moving mirror arm of an interferometer, enables conversion of an FTIR imaging system to discrete frequency imaging. However mid infrared filter devices are still in ongoing development and improvements need to be made before they become widely utilised for discrete frequency imaging in the biomedical field.

Infrared microscopy is inherently a low optical throughput technique since individual spectra are acquired from an area on the micron level. Infrared detectors have improved significantly over the last twenty years, and MCT detectors are now the norm for infrared imaging and have been crucial for spectra to be acquired rapidly with good signal to noise ratios. In contrast to some other detectors, MCT detectors utilising FPA technology are expensive, require cryogenic temperatures to operate and have lengthy stabilisation times. Although these practical limitations are not insurmountable, they serve as yet another barrier to implementation in the clinic. Ever increasing demands are being placed on infrared detector technology, and there is a finite limit on improvements that can be made in the near future. The future direction perhaps lies in improved infrared source technology rather than in detector development. Recent developments in laser technology has led to the introduction of a new family of high intensity infrared sources including free electron lasers (FEL), optical parametric oscillators (OPO) super continuum and quantum cascade lasers (QCL).

Quantum cascade lasers[164] are high intensity, tunable semiconductor lasers which can emit across the mid infrared region of the electromagnetic spectrum. In a conventional semiconductor laser electrons can occupy energy levels in either the valence band or conduction band. Laser emission occurs when high energy electrons in the conduction band undergo an interband transition and combine with holes in the valence band. Emission wavelength depends solely on the band gap and conventional semiconductor lasers are generally not tuneable. QCL's consist of a periodic structure of thin layers of semiconductors with varying composition. In a QCL interband transitions within a quantum well are responsible for the emission. In contrast to conventional semiconductor lasers the electron can then tunnel to an adjacent quantum well where it can undergo a further transition producing further emission. A single electron traversing multiple quantum wells can produce a cascade of photons, and is responsible for QCL high emission intensity and efficiency. Furthermore since the wavelength of emission depends on layer thickness within the device rather than composition, QCL's are tuneable over hundreds of wavenumbers. Availability of these high intensity tunable sources has renewed interest in unmultiplexed, scanning infrared spectrometers utilising discrete frequencies. In contrast to FTIR imaging instruments using thermal sources, highly sensitive infrared detectors are not required due to the high power output of QCL's. Advances in infrared camera technology, in particular micro bolometers, has enabled high resolution, room temperature infrared cameras to become commercially available. Uncooled infrared cameras offer higher pixel density than MCT FPA technology, are more practical and considerably cheaper to manufacture and operate.

To meet the increasing demands of requiring practical, high throughput, high resolution IR chemical imaging instruments, new technology is now becoming commercially available. In a paradigm shift from conventional IR imaging, Daylight Solutions (San Diego, USA) have produced the first commercially available laser based infrared microscope. Utilising four tunable discrete QCL modules as the source enables coverage of the fingerprint region between 900–1800 cm^{-1}. Offering two objectives enables rapid switching between high and medium magnification imaging. A 4× objective allows an area of 2000 μm × 2000 μm to be illuminated, enable a typical TMA biopsy core to be imaged without mapping. Similar measurements with a state of the art FTIR system would require the collection of a 4 × 4 mosaic of infrared tiles, which would then need to be processed and stitched together post collection. High resolution imaging can be performed on regions of interest using the 12× objective on a field of view of 650 μm × 650 μm. Employing a room temperature infrared camera (micro bolometer) enables continuous operation without the practical limitations of cryogenic cooling. Furthermore the high pixel density (480 × 480) of the infrared camera opens up the possibility of high throughput, high resolution chemical imaging utilising a pixel size of only 1.3 μm.

In a recent study[165] a QCL imaging system was used to image a large TMA consisting of 207 breast core biopsies. Using the QCL microscope to collect a chemical image of the amide I band, the full TMA composed of a 10 × 12 array of infrared tiles was collected in just 9 minutes. Measurements on the same sample using a state of the art FTIR FPA system required approximately 19 hours. Although the direct comparison is unfair in that the FTIR collected the full spectral range and the QCL only collected one discrete frequency, the potential speed advantage over FTIR is undeniable, offering the possibility of high throughput imaging of tissue biopsies from a large

numbers of patients. One consideration is the speed of collection for each infrared tile when multiple frequencies are being collected. FTIR utilises the Felgett advantage to collect all wavelengths simultaneous, and sufficient scans are co-added to ensure adequate signal to noise. QCL's are not continuous sources requiring the source to be tuned to the desired wavelength, and data points need to be recorded stepwise for each frequency of interest. Despite this, once spectral biomarkers have been identified the instrument could be assigned to collect a limited number of key features, enabling high throughput imaging. Trials in our own laboratory have demonstrated that high resolution images (1.3 μm pixel size) using 15 features, on a 650 μm × 650 μm area of prostate tissue can be collected in under a minute. Similar measurements using a state of the art FTIR system, albeit with the full spectral range would have taken of the order of an hour. Utilising the medium magnification optics would enable a single core to be collected in under a minute opening up the attractive possibility of real time, high throughput chemical image of large patient tissue biopsies.

While TMA's are a useful research tool, successful clinical translation is likely to require the ability to rapidly image large areas of tissue. We have therefore compared conventional FTIR chemical imaging with high throughput QCL discrete frequency imaging using large area samples obtained from transurethral resections of the prostate (TURP). Imaging a 9.1 mm × 9.1 mm TURP with a conventional FTIR microscope at 8 cm^{-1} resolution with a 5.5 μm pixel size, took approximately 45 minutes to acquire the raw data and a further 45 minutes to process and stitch the tiles together. Fig. 14(a) shows the chemical image based on the intensity of the amide I band. The image is comprised of approximately 3.2 million spectra and there appears to be a high level of detail in the acquired image. The same area was imaged using the QCL system using a pixel size of 1.3 μm but with only five discrete frequencies. The chemical image of the amide I band obtained in approximately two hours is shown in Fig. 14(b). Although the collection times were similar with each instrument, the improved spatial resolution obtained with the QCL system is remarkable. The image in Fig. 14(b) consists of approximately 45 million discrete frequency spectra, enabling rendering of excellent quality high resolution images. As the technology matures it is expected that acquisition times will reduce and large area high definition images could be rapidly obtained.

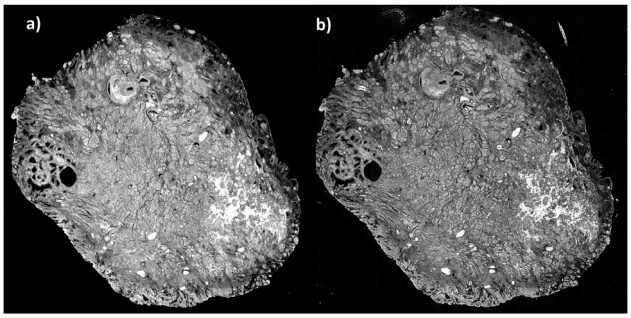

Fig. 14 (a) FT-IR amide I chemical image obtained from a 9.1 mm × 9.1 mm benign prostatic hyperplasia TURP using a 128 × 128 FPA microscope. (b) Corresponding chemical image obtained for the QCL imaging system.

The speed advantage of QCL discrete frequency imaging for interrogating tissue is undeniable, however currently the main focus has been on throughput rather than accurate disease diagnosis. Acceptance of this new technology will depend on whether high quality infrared spectra can be rapidly acquired. Furthermore given that imaging with a QCL system presents a quantum leap in current technology it needs to be demonstrated that infrared spectra similar to those using a conventional FTIR system can be acquired. Despite these exciting developments large scale trials are now required to correctly assess the future of the technology, and its potential in the clinical setting.

In this review we have discussed the developments in infrared spectroscopic imaging for biomedical applications, considered barriers to clinical translation, and highlighted potential solutions. We have demonstrated that SHP has the potential to improve diagnostic accuracy by differentiating between normal and abnormal tissue with high levels of sensitivity and specificity. Currently it is difficult to envisage SHP completely replacing the gold standard of manual examination of H&E stained tissue by a highly trained pathologist. However it is likely that a phased introduction of SHP into the clinical setting could be achieved in the coming years. The possibility of using SHP for identifying abnormal from normal tissue is desirable since it would free up pathologist time for looking at the important (diseased) cases. As confidence grows in SHP and the value which it can add in the clinical setting is recognised, SHP could be used to provide complementary information related to disease diagnosis and prognosis and ultimately improved patient care.

Acknowledgements

PG and MP would like to acknowledge EPSRC (Grant number EP/K02311X/1) and EPSRC UK Network CLIRSPEC (Grant number EP/L012952/1) for support.

References

1 J. B. Lattouf and F. Saad, *BJU Int.*, 2002, **90**, 694–698.
2 Y. Nakai, N. Tanaka, K. Shimada, N. Konishi, M. Miyake, S. Anai and K. Fujimoto, *BMC Urol.*, 2015, **15**, 1–7.
3 L. Gorelick, O. Veksler, M. Gaed, J. A. Gomez, M. Moussa, G. Bauman, A. Fenster and A. D. Ward, *Medical Imaging, IEEE Transactions on*, 2013, **32**, 1804–1818.
4 C. Bahlmann, A. Patel, J. Johnson, J. Ni, A. Chekkoury, P. Khurd, A. Kamen, L. Grady, E. Krupinski, A. Graham and R. Weinstein, *Proc. SPIE, Medical Imaging 2012: Computer-Aided Diagnosis*, 2012, **8315**, 831504.
5 R. Bhargava and R. Kong, *Proc. SPIE 6870, Design and Performance Validation of Phantoms Used in Conjunction with Optical Measurements of Tissue*, 2008, 6870, 687004-687004-687010.

6 P. Chaurand, J. L. Norris, D. S. Cornett, J. A. Mobley and R. M. Caprioli, *J. Proteome Res.*, 2006, **5**, 2889–2900.
7 H. Camp Charles Jr, Y. J. Lee, J. M. Heddleston, C. M. Hartshorn, R. H. WalkerAngela, J. N. Rich, J. D. Lathia and M. T. Cicerone, *Nat. Photonics*, 2014, **8**, 627–634.
8 H. Fabian, P. Lasch, M. Boese and W. Haensch, *Biopolymers*, 2002, **67**, 354–357.
9 H. Fabian, P. Lasch, M. Boese and W. Haensch, *J. Mol. Struct.*, 2003, **661–662**, 411–417.
10 B. R. Wood, L. Chiriboga, H. Yee, M. A. Quinn, D. McNaughton and M. Diem, *Gynecol. Oncol.*, 2004, **93**, 59–68.
11 G. Bellisola and C. Sorio, *Am. J. Cancer Res.*, 2012, **2**, 1–21.
12 M. Diem, A. Mazur, K. Lenau, J. Schubert, B. Bird, M. Miljković, C. Krafft and J. Popp, *J. Biophotonics*, 2013, **6**, 855–886.
13 C. Hughes and M. J. Baker, *Analyst*, 2016, **141**, 467–475.
14 H. J. Byrne, M. Baranska, G. J. Puppels, N. Stone, B. Wood, K. M. Gough, P. Lasch, P. Heraud, J. Sule-Suso and G. D. Sockalingum, *Analyst*, 2015, **140**, 2066–2073.
15 J. A. De Haseth and P. Griffiths, *Fourier Transform Infrared Spectrometry*, 2nd edn, 2007.
16 R. Barer, *Discuss. Faraday Soc.*, 1950, **9**, 369–378.
17 V. J. Coates, A. B. E. Offner and J. E. H. Siegler, *J. Opt. Soc. Am.*, 1953, **43**, 984–989.
18 R. Bhargava and I. W. Levin, *Spectrochemical Analysis Using Infrared Multichannel Detectors*, Blackwell Publishing Ltd, 2007, pp. 1–24.
19 P. Lasch and D. Naumann, *Biochim. Biophys. Acta, Biomembr.*, 2006, **1758**, 814–829.
20 R. Bhargava, *Anal. Bioanal. Chem.*, 2007, **389**, 1155–1169.
21 P. Dumas and L. Miller, *J. Biol. Phys.*, 2003, **29**, 201–218.
22 L. M. Miller and R. J. Smith, *Vib. Spectrosc.*, 2005, **38**, 237–240.
23 P. Dumas and L. Miller, *Vib. Spectrosc.*, 2003, **32**, 3–21.
24 M. J. Tobin, M. A. Chesters, J. M. Chalmers, F. J. M. Rutten, S. E. Fisher, I. M. Symonds, A. Hitchcock, R. Allibone and S. Dias-Gunasekara, *Faraday Discuss.*, 2004, **126**, 27–39.
25 K. Wehbe, A. Travo, S. Eimer, G. Cinque, E. Barron, G. Deleris and I. Forfar, *Anal. Methods*, 2013, **5**, 6925–6932.
26 P. Dumas, G. D. Sockalingum and J. Sulé-Suso, *Trends Biotechnol.*, 2007, **25**, 40–44.
27 A. Marcelli, A. Cricenti, W. M. Kwiatek and C. Petibois, *Biotechnol. Adv.*, 2012, **30**, 1390–1404.
28 S. Ling, Z. Shao and X. Chen, *Prog. Chem.*, 2014, **26**, 178–192.
29 A. V. Rutter, M. R. Siddique, J. Filik, C. Sandt, P. Dumas, G. Cinque, G. D. Sockalingum, Y. Yang and J. Sulé-Suso, *Cytometry, Part A*, 2014, **85**, 688–697.
30 E. Lipiec, G. Birarda, J. Kowalska, J. Lekki, L. Vaccari, A. Wiecheć, B. R. Wood and W. M. Kwiatek, *Radiat. Phys. Chem.*, 2013, **93**, 135–141.
31 I. I. Patel, W. J. Harrison, J. G. Kerns, J. Filik, K. Wehbe, P. L. Carmichael, A. D. Scott, M. P. Philpott, M. D. Frogley, G. Cinque and F. L. Martin, *Anal. Bioanal. Chem.*, 2012, **404**, 1745–1758.
32 J. Pijanka, G. D. Sockalingum, A. Kohler, Y. Yang, F. Draux, G. Parkes, K. P. Lam, D. Collins, P. Dumas, C. Sandt, D. G. Van Pittius, G. Douce, M. Manfait, V. Untereiner and J. Sulé-Suso, *Lab. Invest.*, 2010, **90**, 797–807.
33 C. Hughes, M. Liew, A. Sachdeva, P. Bassan, P. Dumas, C. A. Hart, M. D. Brown, N. W. Clarke and P. Gardner, *Analyst*, 2010, **135**, 3133–3141.
34 J. K. Pijanka, A. Kohler, Y. Yang, P. Dumas, S. Chio-Srichan, M. Manfait, G. D. Sockalingum and J. Sulé-Suso, *Analyst*, 2009, **134**, 1176–1181.
35 *US Pat.*, US 7,378,657 B2, 2008.
36 P. R. Griffiths and E. V. Miseo, *Infrared and Raman Spectroscopic Imaging*, Wiley-VCH Verlag GmbH & Co. KGaA, 2014, pp. 1–56.
37 K. M. Dorling and M. J. Baker, *Trends Biotechnol.*, 2013, **31**, 437–438.
38 P. Bassan, A. Sachdeva, J. H. Shanks, M. D. Brown, N. W. Clarke and P. Gardner, *Analyst*, 2013, **138**, 7066–7069.
39 P. Bassan, A. Sachdeva, J. H. Shanks, M. D. Brown, N. W. Clarke and P. Gardner, *Progress in Biomedical Optics and Imaging - Proceedings of SPIE*, 2014, 9041.
40 C. Beleites, O. Guntinas-Lichius, G. Ernst, J. Popp and C. Krafft, *Biomed. Spectrosc. Imaging*, 2015, **4**, 57–66.
41 N. Wald and E. Goormaghtigh, *Analyst*, 2015, **140**, 2144–2155.
42 X. Mu, M. Kon, A. Ergin, S. Remiszewski, A. Akalin, C. M. Thompson and M. Diem, *Analyst*, 2015, **140**, 2449–2464.
43 F. Großerueschkamp, A. Kallenbach-Thieltges, T. Behrens, T. Brüning, M. Altmayer, G. Stamatis, D. Theegarten and K. Gerwert, *Analyst*, 2015, **140**, 2114–2120.
44 J. Nallala, M.-D. Diebold, C. Gobinet, O. Bouche, G. D. Sockalingum, O. Piot and M. Manfait, *Analyst*, 2014, **139**, 4005–4015.
45 B. Bird, M. Miljkovi, S. Remiszewski, A. Akalin, M. Kon and M. Diem, *Lab. Invest.*, 2012, **92**, 1358–1373.
46 F. Ghaznavi, A. Evans, A. Madabhushi and M. Feldman, *Annu. Rev. Pathol.: Mech. Dis.*, 2013, **8**, 331–359.
47 C. S. Colley, S. G. Kazarian, P. D. Weinberg and M. J. Lever, *Biopolymers*, 2004, **74**, 328–335.
48 F. Palombo, H. Shen, L. E. S. Benguigui, S. G. Kazarian and R. K. Upmacis, *Analyst*, 2009, **134**, 1107–1118.
49 M. K. Kuimova, K. L. A. Chan and S. G. Kazarian, *Appl. Spectrosc.*, 2009, **63**, 164–171.
50 K. L. A. Chan and S. G. Kazarian, *Appl. Spectrosc.*, 2003, **57**, 381–389.
51 C. Ricci, S. Bloxham and S. G. Kazarian, *Journal of Cultural Heritage*, 2007, **8**, 387–395.
52 K. L. A. Chan, S. V. Hammond and S. G. Kazarian, *Anal. Chem.*, 2003, **75**, 2140–2146.
53 K. L. A. Chan, S. G. Kazarian, A. Mavraki and D. R. Williams, *Appl. Spectrosc.*, 2005, **59**, 149–155.
54 M. J. Walsh, S. E. Holton, A. Kajdacsy-Balla and R. Bhargava, *Vib. Spectrosc.*, 2012, **60**, 23–28.
55 M. J. Walsh, D. Mayerich, A. Kajdacsy-Balla and R. Bhargava, *Proc. SPIE 8219, Biomedical Vibrational Spectroscopy V: Advances in Research and Industry*, 2012, 82190R–82199R.
56 J. A. Reffner, P. A. Martoglio and G. P. Williams, *Rev. Sci. Instrum.*, 1995, **66**, 1298–1302.

57 D. Moss, B. Gasharova and Y.-L. Mathis, *Infrared Phys. Technol.*, 2006, **49**, 53–56.
58 M. J. Nasse, E. C. Mattson, R. Reininger, T. Kubala, S. Janowski, Z. El-Bayyari and C. J. Hirschmugl, *Nucl. Instrum. Methods Phys. Res., Sect. A*, 2011, **649**, 172–176.
59 M. J. Nasse, M. J. Walsh, E. C. Mattson, R. Reininger, A. Kajdacsy-Balla, V. Macias, R. Bhargava and C. J. Hirschmugl, *Nat. Methods*, 2011, **8**, 413–416.
60 C. R. Liao, M. Rak, J. Lund, M. Unger, E. Platt, B. C. Albensi, C. J. Hirschmugl and K. M. Gough, *Analyst*, 2013, **138**, 3991–3997.
61 E. Stavitski, R. J. Smith, M. W. Bourassa, A. S. Acerbo, G. L. Carr and L. M. Miller, *Anal. Chem.*, 2013, **85**, 3599–3605.
62 L. S. Leslie, A. Kadjacsy-Balla, R. Bhargava, *Proc. SPIE, Medical Imaging, 2015: Digital Pathology*, 2015, **9420**, 94200I–94208I.
63 P. Bassan, J. Mellor, J. Shapiro, K. J. Williams, M. P. Lisanti and P. Gardner, *Anal. Chem.*, 2014, **86**, 1648–1653.
64 E. C. Mattson, M. Unger, S. Clede, F. Lambert, C. Policar, A. Imtiaz, R. D'Souza and C. J. Hirschmugl, *Analyst*, 2013, **138**, 5610–5618.
65 S. Clede, F. Lambert, C. Sandt, S. Kascakova, M. Unger, E. Harte, M.-A. Plamont, R. Saint-Fort, A. Deniset-Besseau, Z. Gueroui, C. Hirschmugl, S. Lecomte, A. Dazzi, A. Vessieres and C. Policar, *Analyst*, 2013, **138**, 5627–5638.
66 M. J. Nasse, B. Bellehumeur, S. Ratti, C. Olivieri, D. Buschke, J. Squirrell, K. Eliceiri, B. Ogle, C. S. Patterson, M. Giordano and C. J. Hirschmugl, *Vib. Spectrosc.*, 2012, **60**, 10–15.
67 M. J. Tobin, L. Puskar, R. L. Barber, E. C. Harvey, P. Heraud, B. R. Wood, K. R. Bambery, C. T. Dillon and K. L. Munro, *Vib. Spectrosc.*, 2010, **53**, 34–38.
68 P. Gelfand, R. J. Smith, E. Stavitski, D. R. Borchelt and L. M. Miller, *Anal. Chem.*, 2015, **87**, 6025–6031.
69 K. R. Flower, I. Khalifa, P. Bassan, D. Demoulin, E. Jackson, N. P. Lockyer, A. T. McGown, P. Miles, L. Vaccari and P. Gardner, *Analyst*, 2011, **136**, 498–507.
70 L. Vaccari, G. Birarda, L. Businaro, S. Pacor and G. Grenci, *Anal. Chem.*, 2012, **84**, 4768–4775.
71 G. Clemens, K. R. Flower, A. P. Henderson, A. Whiting, S. A. Przyborski, M. Jimenez-Hernandez, F. Ball, P. Bassan, G. Cinque and P. Gardner, *Mol. BioSyst.*, 2013, **9**, 677–692.
72 B. J. Davis, P. S. Carney and R. Bhargava, *Anal. Chem.*, 2010, **82**, 3474–3486.
73 B. J. Davis, P. S. Carney and R. Bhargava, *Anal. Chem.*, 2010, **82**, 3487–3499.
74 R. K. Reddy, M. J. Walsh, M. V. Schulmerich, P. S. Carney and R. Bhargava, *Appl. Spectrosc.*, 2013, **67**, 93–105.
75 R. Reddy, D. Mayerich, M. Walsh, M. Schulmerich, P. S. Carney and R. Bhargava, *Biomedical Imaging (ISBI), 2012 9th IEEE International Symposium on*, 2012, 354–357.
76 A. A. Green, M. Berman, P. Switzer and M. D. Craig, *IEEE Transactions on Geoscience and Remote Sensing*, 1988, **26**, 65–74.
77 C. R. Findlay, R. Wiens, M. Rak, J. Sedlmair, C. J. Hirschmugl, J. Morrison, C. J. Mundy, M. Kansiz and K. M. Gough, *Analyst*, 2015, **140**, 2493–2503.
78 C. Hughes, A. Henderson, M. Kansiz, K. M. Dorling, M. Jimenez-Hernandez, M. D. Brown, N. W. Clarke and P. Gardner, *Analyst*, 2015, **140**, 2080–2085.
79 H. M. Pollock and A. Hammiche, *J. Phys. D: Appl. Phys.*, 2001, **34**, R23–R53.
80 A. Hammiche, H. M. Pollock, M. Reading, M. Claybourn, P. H. Turner and K. Jewkes, *Appl. Spectrosc.*, 1999, **53**, 810–815.
81 A. Dazzi, R. Prazeres, F. Glotin and J. M. Ortega, *Opt. Lett.*, 2005, **30**, 2388–2390.
82 A. Dazzi, F. Glotin and R. Carminati, *J. Appl. Phys.*, 2010, **107**, 124519.
83 W. I. Gruszecki, A. J. Kulik, E. Janik, J. Bednarska, R. Luchowski, W. Grudzinski and G. Dietler, *Nanoscale*, 2015, **7**, 14659–14662.
84 K. Vodopyanov, G. A. Hill, J. H. Rice, S. R. Meech, D. Q. M. Craig, M. M. Reading, A. Dazzi, K. Kjoller and C. Prater, *Frontiers in Optics 2009/Laser Science XXV/Fall 2009 OSA Optics & Photonics Technical Digest*, 2009, FMK2.
85 F. Lu and M. A. Belkin, *Opt. Express*, 2011, **19**, 19942–19947.
86 A. Dazzi, J. Saunier, K. Kjoller and N. Yagoubi, *Int. J. Pharm.*, 2015, **484**, 109–114.
87 A. Dazzi, C. B. Prater, Q. Hu, D. B. Chase, J. F. Rabolt and C. Marcott, *Appl. Spectrosc.*, 2012, **66**, 1365–1384.
88 R. H. F. Keilmann, *Philos. Trans. R. Soc. London, Ser. A*, 2004, **362**, 785–805.
89 F. Huth, M. Schnell, J. Wittborn, N. Ocelic and R. Hillenbrand, *Nat. Mater.*, 2011, **10**, 352–356.
90 F. Huth, A. Govyadinov, S. Amarie, W. Nuansing, F. Keilmann and R. Hillenbrand, *Nano Lett.*, 2012, **12**, 3973–3978.
91 E. Yoxall, M. Schnell, S. Mastel and R. Hillenbrand, *Opt. Express*, 2015, **23**, 13358–13369.
92 E. A. Muller, R. L. Olmon, H. A. Bechtela, M. C. Martina and M. B. Raschkeb, *Proc. Natl. Acad. Sci. U. S. A.*, 2014, **111**, 7191–7196.
93 A. D. Smith, M. R. F. Siggel-King, G. M. Holder, A. Cricenti, M. Luce, P. Harrison, D. S. Martin, M. Surman, T. Craig, S. D. Barrett, A. Wolski, D. J. Dunning, N. R. Thompson, Y. Saveliev, D. M. Pritchard, A. Varro, S. Chattopadhyay and P. Weightman, *Appl. Phys. Lett.*, 2013, **102**, 053701.
94 J. Filik, M. D. Frogley, J. K. Pijanka, K. Wehbe and G. Cinque, *Analyst*, 2012, **137**, 853–861.
95 H. Brooke, D. L. Perkins, B. Setlow, P. Setlow, B. V. Bronk and M. L. Myrick, *Appl. Spectrosc.*, 2008, **62**, 881–888.
96 P. Bassan, J. Lee, A. Sachdeva, J. Pissardini, K. M. Dorling, J. S. Fletcher, A. Henderson and P. Gardner, *Analyst*, 2013, **138**, 144–157.
97 T. P. Wrobel, B. Wajnchold, H. J. Byrne and M. Baranska, *Vib. Spectrosc.*, 2013, **69**, 84–92.
98 M. Miljkovic, B. Bird, K. Lenau, A. I. Mazur and M. Diem, *Analyst*, 2013, **138**, 3975–3982.
99 J. Cao, E. S. Ng, D. McNaughton, E. G. Stanley, A. G. Elefanty, M. J. Tobin and P. Heraud, *Analyst*, 2013, **138**, 4147–4160.
100 K. Kochan, P. Heraud, M. Kiupel, V. Yuzbasiyan-Gurkan, D. McNaughton, M. Baranska and B. R. Wood, *Analyst*, 2015, **140**, 2402–2411.
101 J. A. Cohen and C. Virnelson, *US Pat.*, 5160826, 1991.

102 R. G. Greenler, *J. Chem. Phys.*, 1966, **44**, 310–315.
103 A. Anthony, G. J. Colurso, T. M. A. Bocan and J. A. Doebler, *Histochem. J.*, 1984, **16**, 61–70.
104 M. J. Pilling, P. Bassan and P. Gardner, *Analyst*, 2015, **140**, 2383–2392.
105 S. Boydston-White, M. Romeo, T. Chernenko, A. Regina, M. Miljković and M. Diem, *Biochim. Biophys. Acta, Biomembr.*, 2006, **1758**, 908–914.
106 C. Hughes, M. D. Brown, F. J. Ball, G. Monjardez, N. W. Clarke, K. R. Flower and P. Gardner, *Analyst*, 2012, **137**, 5736–5742.
107 M. Jimenez-Hernandez, C. Hughes, P. Bassan, F. Ball, M. D. Brown, N. W. Clarke and P. Gardner, *Analyst*, 2013, **138**, 3957–3966.
108 M. Jimenez-Hernandez, M. D. Brown, C. Hughes, N. W. Clarke and P. Gardner, *Analyst*, 2015, **140**, 4453–4464.
109 M. Romeo, B. Mohlenhoff and M. Diem, *Vib. Spectrosc.*, 2006, **42**, 9–14.
110 A. Kohler, J. Sulé-Suso, G. D. Sockalingum, M. Tobin, F. Bahrami, Y. Yang, J. Pijanka, P. Dumas, M. Cotte, D. G. van Pittius, G. Parkes and H. Martens, *Appl. Spectrosc.*, 2008, **62**, 259–266.
111 P. Bassan, H. J. Byrne, F. Bonnier, J. Lee, P. Dumas and P. Gardner, *Analyst*, 2009, **134**, 1586–1593.
112 H. C. v. d. Hulst, *Light scattering by small particles*, Dover Publications, Mineola, NY, 1981.
113 P. Bassan, A. Kohler, H. Martens, J. Lee, H. J. Byrne, P. Dumas, E. Gazi, M. Brown, N. Clarke and P. Gardner, *Analyst*, 2010, **135**, 268–277.
114 P. Bassan, A. Kohler, H. Martens, J. Lee, E. Jackson, N. Lockyer, P. Dumas, M. Brown, N. Clarke and P. Gardner, *J. Biophotonics*, 2010, **3**, 609–620.
115 K. R. Bambery, B. R. Wood and D. McNaughton, *Analyst*, 2012, **137**, 126–132.
116 P. Bassan, H. J. Byrne, J. Lee, F. Bonnier, C. Clarke, P. Dumas, E. Gazi, M. D. Brown, N. W. Clarke and P. Gardner, *Analyst*, 2009, **134**, 1171–1175.
117 P. Bassan, A. Sachdeva, A. Kohler, C. Hughes, A. Henderson, J. Boyle, J. H. Shanks, M. Brown, N. W. Clarke and P. Gardner, *Analyst*, 2012, **137**, 1370–1377.
118 M. Miljkovic, B. Bird and M. Diem, *Analyst*, 2012, **137**, 3954–3964.
119 A. Dazzi, A. Deniset-Besseau and P. Lasch, *Analyst*, 2013, **138**, 4191–4201.
120 C. Hughes, L. Gaunt, M. Brown, N. W. Clarke and P. Gardner, *Anal. Methods*, 2014, **6**, 1028–1035.
121 E. Ly, O. Piot, R. Wolthuis, A. Durlach, P. Bernard and M. Manfait, *Analyst*, 2008, **133**, 197–205.
122 A. Travo, O. Piot, R. Wolthuis, C. Gobinet, M. Manfait, J. Bara, M.-E. Forgue-Lafitte and P. Jeannesson, *Histopathology*, 2010, **56**, 921–931.
123 D. Sebiskveradze, V. Vrabie, C. Gobinet, A. Durlach, P. Bernard, E. Ly, M. Manfait, P. Jeannesson and O. Piot, *Lab. Invest.*, 2011, **91**, 799–811.
124 T. T. Nguyen, C. Eklouh-Molinier, D. Sebiskveradze, J. Feru, C. Terryn, M. Manfait, S. Brassart-Pasco and O. Piot, *Analyst*, 2014, **139**, 2482–2488.
125 C. Gobinet, D. Sebiskveradze, V. Vrabie, A. Tfayli, O. Piot and M. Manfait, *Signal Processing Conference, 2008 16th European*, 2008, 1–5.
126 D. Sebiskveradze, C. Gobinet, E. Ly, M. Manfait, P. Jeannesson, M. Herbin, O. Piot and V. Vrabie, *BioInformatics and BioEngineering, 2008. BIBE 2008. 8th IEEE International Conference on*, 2008, 1–6.
127 M. J. Hackett, J. Lee, F. El-Assaad, J. A. McQuillan, E. A. Carter, G. E. Grau, N. H. Hunt and P. A. Lay, *ACS Chem. Neurosci.*, 2012, **3**, 1017–1024.
128 W. C. E. Stewart BW, World Cancer Report, WHO Press, 2014.
129 J. G. Elmore, G. M. Longton and P. A. Carney, *et al.*, *JAMA, J. Am. Med. Assoc.*, 2015, **313**, 1122–1132.
130 D. L. Weaver, R. D. Rosenberg, W. E. Barlow, L. Ichikawa, P. A. Carney, K. Kerlikowske, D. S. M. Buist, B. M. Geller, C. R. Key, S. J. Maygarden and R. Ballard-Barbash, *Cancer*, 2006, **106**, 732–742.
131 M. J. Baker, E. Gazi, M. D. Brown, J. H. Shanks, N. W. Clarke and P. Gardner, *J. Biophotonics*, 2009, **2**, 104–113.
132 M. J. Baker, E. Gazi, M. D. Brown, J. H. Shanks, P. Gardner and N. W. Clarke, *Br. J. Cancer*, 2008, **99**, 1859–1866.
133 E. Gazi, M. Baker, J. Dwyer, N. P. Lockyer, P. Gardner, J. H. Shanks, R. S. Reeve, C. A. Hart, N. W. Clarke and M. D. Brown, *Eur. Urol.*, 2006, **50**, 750–761.
134 E. Gazi, J. Dwyer, N. Lockyer, P. Gardner, J. C. Vickerman, J. Miyan, C. A. Hart, M. Brown, J. H. Shanks and N. Clarke, *Faraday Discuss.*, 2004, **126**, 41–59.
135 D. C. Fernandez, R. Bhargava, S. M. Hewitt and I. W. Levin, *Nat. Biotechnol.*, 2005, **23**, 469–474.
136 M. A. Mackanos and C. H. Contag, *Trends Biotechnol.*, 2009, **27**, 661–663.
137 J. T. Kwak, A. Kajdacsy-Balla, V. Macias, M. Walsh, S. Sinha and R. Bhargava, *Sci. Rep.*, 2015, **5**, 8758.
138 N. Bergner, B. F. M. Romeike, R. Reichart, R. Kalff, C. Krafft and J. Popp, *Analyst*, 2013, **138**, 3983–3990.
139 R. Noreen, M. Moenner, Y. Hwu and C. Petibois, *Biotechnol. Adv.*, 2012, **30**, 1432–1446.
140 S. B. Sobottka, K. D. Geiger, R. Salzer, G. Schackert and C. Krafft, *Anal. Bioanal. Chem.*, 2009, **393**, 187–195.
141 C. Beleites, G. Steiner, M. G. Sowa, R. Baumgartner, S. Sobottka, G. Schackert and R. Salzer, *Vib. Spectrosc.*, 2005, **38**, 143–149.
142 V. Sablinskas, G. Steiner, E. Koch, J. Ceponkus, M. Pucetaite, S. Strazdaite, V. Urboniene and F. Jankevicius, *Progress in Biomedical Optics and Imaging - Proceedings of SPIE*, 2011, 7902.
143 A. Akalin, X. Mu, M. A. Kon, A. Ergin, S. H. Remiszewski, C. M. Thompson, D. J. Raz and M. Diem, *Lab. Invest.*, 2015, **95**, 406–421.
144 A. Tfayli, O. Piot, A. Durlach, P. Bernard and M. Manfait, *Biochim. Biophys. Acta, Gen. Subj.*, 2005, **1724**, 262–269.
145 Z. Hammody, S. Argov, R. K. Sahu, E. Cagnano, R. Moreh and S. Mordechai, *Analyst*, 2008, **133**, 372–378.
146 A. Kallenbach-Thieltges, F. Großerüschkamp, A. Mosig, M. Diem, A. Tannapfel and K. Gerwert, *J. Biophotonics*, 2013, **6**, 88–100.

147 B. Bird, K. Bedrossian, N. Laver, M. Miljković, M. J. Romeo and M. Diem, *Analyst*, 2009, **134**, 1067–1076.
148 H. Fabian, N. A. N. Thi, M. Eiden, P. Lasch, J. Schmitt and D. Naumann, *Biochim. Biophys. Acta, Biomembr.*, 2006, **1758**, 874–882.
149 G. J. Ooi, J. Fox, K. Siu, R. Lewis, K. R. Bambery, D. McNaughton and B. R. Wood, *Med. Phys.*, 2008, **35**, 2151–2161.
150 J. V. Coe, Z. Chen, R. Li, R. Butke, B. Miller, C. L. Hitchcock, H. C. Allen, S. P. Povoski and E. W. Martin, *Proc. SPIE 8947, Imaging, Manipulation, and Analysis of Biomolecules, Cells, and Tissues XII*, 2014, 8947, 89470B-89470B-89476.
151 C. Pezzei, A. Brunner, G. K. Bonn and C. W. Huck, *Analyst*, 2013, **138**, 5719–5725.
152 C. Hughes, J. Iqbal-Wahid, M. Brown, J. H. Shanks, A. Eustace, H. Denley, P. J. Hoskin, C. West, N. W. Clarke and P. Gardner, *J. Biophotonics*, 2013, **6**, 73–87.
153 M. Griebe, M. Daffertshofer, M. Stroick, M. Syren, P. Ahmad-Nejad, M. Neumaier, J. Backhaus, M. G. Hennerici and M. Fatar, *Neurosci. Lett.*, 2007, **420**, 29–33.
154 C. Beleites, U. Neugebauer, T. Bocklitz, C. Krafft and J. Popp, *Anal. Chim. Acta*, 2013, **760**, 25–33.
155 P. Lasch, M. Diem, W. Hänsch and D. Naumann, *J. Chemom.*, 2007, **20**, 209–220.
156 J. Kononen, L. Bubendorf, A. Kallionimeni, M. Barlund, P. Schraml, S. Leighton, J. Torhorst, M. J. Mihatsch, G. Sauter and O.-P. Kallionimeni, *Nat. Med.*, 1998, **4**, 844–847.
157 A. C. Williams, B. W. Barry, H. G. Edwards and D. W. Farwell, *Pharm. Res.*, 1993, **10**, 1642–1647.
158 A. M. DeMarzo, W. G. Nelson, W. B. Isaacs and J. I. Epstein, *Lancet*, 2003, **361**, 955–964.
159 S. Kumar, C. Desmedt, D. Larsimont, C. Sotiriou and E. Goormaghtigh, *Analyst*, 2013, **138**, 4058–4065.
160 R. Kong, R. K. Reddy and R. Bhargava, *Analyst*, 2010, **135**, 1569–1578.
161 S. E. Holton, M. J. Walsh and R. Bhargava, *Analyst*, 2011, **136**, 2953–2958.
162 A. Ergin, F. Großerüschkamp, O. Theisen, K. Gerwert, S. Remiszewski, C. M. Thompson and M. Diem, *Analyst*, 2015, **140**, 2465–2472.
163 S. W. Bruun, A. Kohler, I. Adt, G. D. Sockalingum, M. Manfait and H. Martens, *Appl. Spectrosc.*, 2006, **60**, 1029–1039.
164 J. Faist, F. Capasso, D. L. Sivco, C. Sirtori, A. L. Hutchinson and A. Y. Cho, *Science*, 1994, **264**, 553–556.
165 P. Bassan, M. J. Weida, J. Rowlette and P. Gardner, *Analyst*, 2014, **139**, 3856–3859.